RESEARCH ARTICLE SUMMARY

ADVANCED IMAGING

Lattice light-sheet microscopy: Imaging molecules to embryos at high spatiotemporal resolution

Bi-Chang Chen, Wesley R. Legant, Kai Wang, Lin Shao, Daniel E. Milkie, Michael W. Davidson, Chris Janetopoulos, Xufeng S. Wu, John A. Hammer III, Zhe Liu, Brian P. English, Yuko Mimori-Kiyosue, Daniel P. Romero, Alex T. Ritter, Jennifer Lippincott-Schwartz, Lillian Fritz-Laylin, R. Dyche Mullins, Diana M. Mitchell, Joshua N. Bembenek, Anne-Cecile Reymann, Ralph Böhme, Stephan W. Grill, Jennifer T. Wang, Geraldine Seydoux, U. Serdar Tulu, Daniel P. Kiehart, Eric Betzig*

INTRODUCTION: In vivo imaging provides a window into the spatially complex, rapidly evolving physiology of the cell that structural imaging alone cannot. However, observing this physiology directly involves inevitable tradeoffs of spatial resolution, temporal resolution, and phototoxicity. This is especially true when imaging in three dimensions, which is essential to obtain a complete picture of many dynamic subcellular processes. Although traditional in vivo imaging tools, such as widefield and confocal microscopy, and newer ones, such as light-sheet microscopy, can image in three dimensions, they sacrifice substantial spatiotemporal resolution to do so and, even then, can often be used for only very limited durations before altering the physiological state of the specimen.

RATIONALE: To address these limitations, we developed a new microscope using ultrathin light sheets derived from two-dimensional (2D) optical lattices. These are scanned plane-by-plane through the specimen to generate a 3D image. The thinness of the sheet leads to high axial resolution and negligible photobleaching and background outside of the focal plane, while its simultaneous illumination of the entire field of view permits imaging at hundreds of planes per second even at extremely low peak excitation intensities. By implementing either superresolution structured illumination or by dithering the lattice to create a uniform light sheet, we imaged cells and small embryos in three dimensions, often at subsecond intervals, for hundreds to thousands of time points at the diffraction limit and beyond.

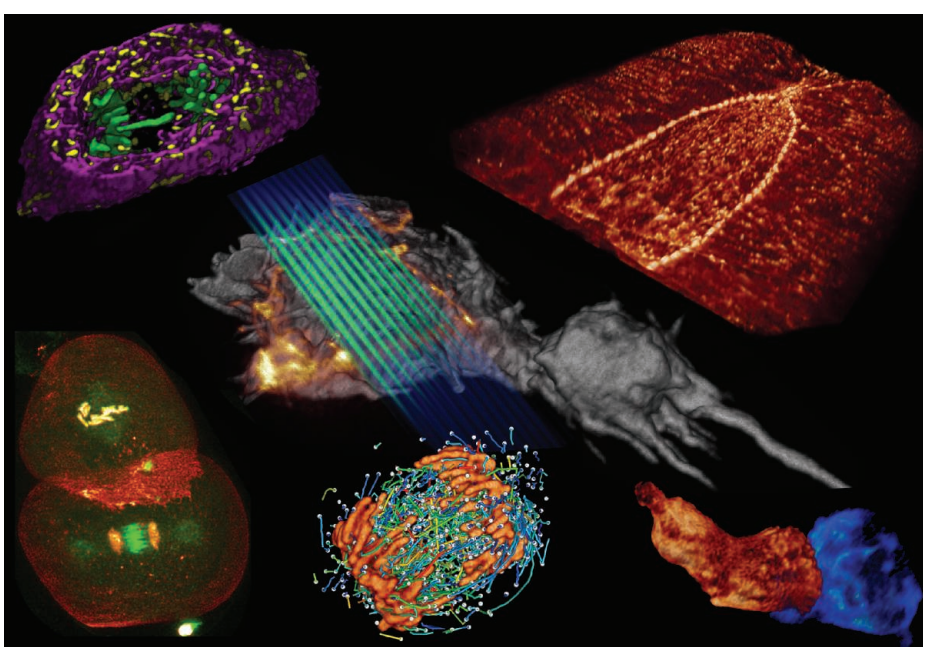

Lattice light-sheet microscopy. An ultrathin structured light sheet (blue-green, center) excites fluorescence (orange) in successive planes as it sweeps through a specimen (gray) to generate a 3D image. The speed, noninvasiveness, and high spatial resolution of this approach make it a promising tool for in vivo 3D imaging of fast dynamic processes in cells and embryos, as shown here in five surrounding examples.

RESULTS: We demonstrated the technique on 20 different biological processes spanning four orders of magnitude in space and time, including the binding kinetics of single Sox2 transcription factor molecules, 3D superresolution photoactivated localization microscopy of nuclear lamins, dynamic organelle rearrangements and 3D tracking of microtubule plus ends during mitosis, neutrophil motility in a collagen mesh, and subcellular protein localization and dynamics during embryogenesis in *Caenorhabditis elegans* and *Drosophila melanogaster*. Throughout, we established the performance advantages of lattice light-sheet microscopy compared with previous techniques and highlighted phenomena that, when seen at increased spatiotemporal detail, may hint at previously unknown biological mechanisms.

ON OUR WEB SITE

Read the full article at http://dx.doi.org/10.1126/science.1257998

CONCLUSION: Photobleaching and phototoxicity are typically reduced by one to two orders of magnitude relative to that seen with a 1D scanned Bessel beam or the point array scanned excitation of spinning disk confocal microscopy. This suggests that the instantaneous peak power delivered to the specimen may be an even more important metric of cell health than the total photon dose and should enable extended 3D observation of endogenous levels of even sparsely expressed proteins produced by genome editing. Improvements of similar magnitude in imaging speed and a twofold gain in axial resolution relative to confocal microscopy yield 4D spatiotemporal resolution high enough to follow fast, nanoscale dynamic processes that would otherwise be obscured by poor resolution along one or more axes of spacetime. Last, the negligible background makes lattice light-sheet microscopy a promising platform for the extension of all methods of superresolution to larger and more densely fluorescent specimens and enables the study of signaling, transport, and stochastic self-assembly in complex environments with single-molecule sensitivity. ■

The list of author affiliations is available in the full article online.
***Corresponding author. E-mail: betzige@janelia.hhmi.org**
Cite this article as B.-C. Chen *et al.*, *Science* **346**, 1257998 (2014). DOI: 10.1126/science.1257998

Corrected 30 January 2015; see full text.

Published by AAAS

RESEARCH ARTICLE

ADVANCED IMAGING

Lattice light-sheet microscopy: Imaging molecules to embryos at high spatiotemporal resolution

Bi-Chang Chen,[1*†] Wesley R. Legant,[1*] Kai Wang,[1*] Lin Shao,[1] Daniel E. Milkie,[2] Michael W. Davidson,[3] Chris Janetopoulos,[4] Xufeng S. Wu,[5] John A. Hammer III,[5] Zhe Liu,[1] Brian P. English,[1] Yuko Mimori-Kiyosue,[6] Daniel P. Romero,[7] Alex T. Ritter,[8,9] Jennifer Lippincott-Schwartz,[8] Lillian Fritz-Laylin,[10] R. Dyche Mullins,[10] Diana M. Mitchell,[11‡] Joshua N. Bembenek,[11] Anne-Cecile Reymann,[12,13§] Ralph Böhme,[12,13] Stephan W. Grill,[12,13§] Jennifer T. Wang,[14] Geraldine Seydoux,[14] U. Serdar Tulu,[15] Daniel P. Kiehart,[15] Eric Betzig[1||]

Although fluorescence microscopy provides a crucial window into the physiology of living specimens, many biological processes are too fragile, are too small, or occur too rapidly to see clearly with existing tools. We crafted ultrathin light sheets from two-dimensional optical lattices that allowed us to image three-dimensional (3D) dynamics for hundreds of volumes, often at subsecond intervals, at the diffraction limit and beyond. We applied this to systems spanning four orders of magnitude in space and time, including the diffusion of single transcription factor molecules in stem cell spheroids, the dynamic instability of mitotic microtubules, the immunological synapse, neutrophil motility in a 3D matrix, and embryogenesis in *Caenorhabditis elegans* and *Drosophila melanogaster*. The results provide a visceral reminder of the beauty and the complexity of living systems.

The hallmark of life is that it is animate. Every living thing is a complex thermodynamic pocket of reduced entropy through which matter and energy flow continuously. Thus, although structural imaging is certainly informative, a more-complete understanding of how inanimate molecules assemble to create animate life requires high-resolution imaging across all four dimensions of spacetime simultaneously.

The problem is that the twin goals of high spatial resolution to see fine structural detail and high temporal resolution to follow fast dynamical processes are mutually opposed to one another: Increased spatial resolution requires more measurements, takes more time, and pumps more potentially damaging radiation into the specimen.

Fortunately, the most common tools used for in vivo molecular and organelle-specific imaging, widefield and confocal fluorescence microscopy (*1*, *2*), leave substantial room for improvement, because they each illuminate the entire thickness of the specimen, even though high-resolution information is obtained from only a single focal plane. This results in premature photobleaching and phototoxicity, limiting the duration of the imaging and altering the physiological state of the specimen.

A notable exception in this regard is light-sheet microscopy (*3*, *4*), which uses a separate excitation lens perpendicular to the widefield detection lens to confine the illumination to the neighborhood of the focal plane. This approach has proven powerful for noninvasive four-dimensional (4D) imaging of embryos at single-cell resolution (*5*, *6*); however, conventional light sheets created with Gaussian beams (Fig. 1A) are too thick over cellular dimensions to benefit subcellular imaging. In response, we introduced (*7*) "nondiffracting" Bessel beams to light sheet microscopy (Fig. 1B): When swept across the imaging focal plane, such a beam creates a virtual light sheet of submicrometer thickness well suited to noninvasive high-speed 4D live cell imaging.

In a more-recent implementation (*8*) that exploits the principles of 3D superresolution structured illumination microscopy (SIM) (*9*) for further resolution enhancement, we used a linear array of seven parallel, noninteracting Bessel beams to compensate for the additional acquisition time that SIM requires. To our surprise, we found this multiple-beam approach to be much less phototoxic than a single beam for the same total power delivered to the sample. Similar effects have been observed in spinning disk confocal microscopy (*10*), where the excitation is spread across many foci, greatly reducing the intensity at any single focus and in turn reducing the effect of nonlinear photodamage mechanisms. We therefore decided to explore means to create a thin, nondiffracting light sheet of low intensity, spread across a broad area, which would offer further gains in speed and noninvasiveness.

Lattice light sheets: Theory and performance

Our approach begins with a 2D optical lattice. Optical lattices are periodic interference patterns in two or three dimensions created by the coherent superposition of a finite number of plane waves traveling in certain well-defined directions (*11*, *12*) (fig. S1) and have been used to trap and cool atoms (*13*) or to fabricate nanolithographic structures (*14*). Like an ideal Bessel beam, an ideal 2D lattice is nondiffracting in the sense that it propagates indefinitely in a direction y without changing its cross-sectional profile, which extends infinitely in x and z. In either case, this is accomplished by confining the illumination at the rear pupil plane of the excitation objective to points on an infinitesimally thin ring. In practice, it is necessary to replace this ring with an annulus of finite thickness and to control the thickness of the annulus to confine the pattern in z, thereby producing a sheet rather than a block of light. However, this also reduces the extent in y over which the pattern is uniform, so there is a tradeoff between the thinness of the light sheet and its effective field of view in y. In the case of a Bessel beam restricted in y to cover the field of view of a typical cultured cell, there is enough energy remaining in side lobes concentric to the central beam to create substantial out-of-focus background in z when the beam is swept in x (Fig. 1B). On the other hand, we have identified (supplementary note 1) numerous 2D optical lattices that, over a similar field of view, can be optimized to either confine the excitation (*15*) tightly to the xy plane (Fig. 1C), maximize the z resolution (Fig. 1D and fig. S2) defined by the overall point spread function (PSF) of the microscope, or provide superresolution in the xz plane by SIM (fig. S3).

To create these lattices, we started with an optical path that is (fig. S4) conceptually similar to our earlier Bessel microscope (*7*, *8*). To this, we added a fast switching spatial light modulator (SLM) conjugated to the sample plane and placed before the annular mask. We write the xz cross-sectional electric field amplitude of the desired theoretical

[1]Janelia Research Campus, Howard Hughes Medical Institute, Ashburn, VA 20147, USA. [2]Coleman Technologies, Incorporated, Newtown Square, PA 19073, USA. [3]National High Magnetic Field Laboratory and Department of Biological Science, Florida State University, Tallahassee, FL 32310, USA. [4]Department of Biological Sciences, University of the Sciences, Philadelphia, PA 19104, USA. [5]Laboratory of Cell Biology, National Heart, Lung, and Blood Institute, National Institutes of Health, Bethesda, MD 20892, USA. [6]Optical Image Analysis Unit, RIKEN Center for Developmental Biology, Kobe 650-0047, Japan. [7]Department of Pharmacology, University of Minnesota, Minneapolis, MN 55455, USA. [8]Cell Biology and Metabolism Program, National Institute of Child Health and Human Development, National Institutes of Health, Bethesda, MD 20892, USA. [9]Cambridge Institute for Medical Research, Addenbrooke's Hospital, Cambridge CB2 0XY, England, UK. [10]Department of Cellular and Molecular Pharmacology, University of California, San Francisco, San Francisco, CA 94158, USA. [11]Department of Biochemistry and Cellular and Molecular Biology, University of Tennessee, Knoxville, TN 37996, USA. [12]Max Planck Institute for Molecular Cell Biology and Genetics, 01307 Dresden, Germany. [13]Max Planck Institute for the Physics of Complex Systems, 01307 Dresden, Germany. [14]Department of Molecular Biology and Genetics, Howard Hughes Medical Institute, Center for Cell Dynamics, Johns Hopkins School of Medicine, Baltimore, MD 21205, USA. [15]Department of Biology, Duke University, Durham, NC 27708, USA.
*These authors contributed equally to this work. †Present address: Research Center for Applied Sciences, Academica Sinica, Taipei 115-29, Taiwan. ‡Present address: Department of Biological Sciences, University of Idaho, Moscow, ID 83844, USA. §Present address: BIOTEC, Technische Universität Dresden, 01307 Dresden, Germany. ||Corresponding author. E-mail: betzige@janelia.hhmi.org

Corrected 30 January 2015; see full text.

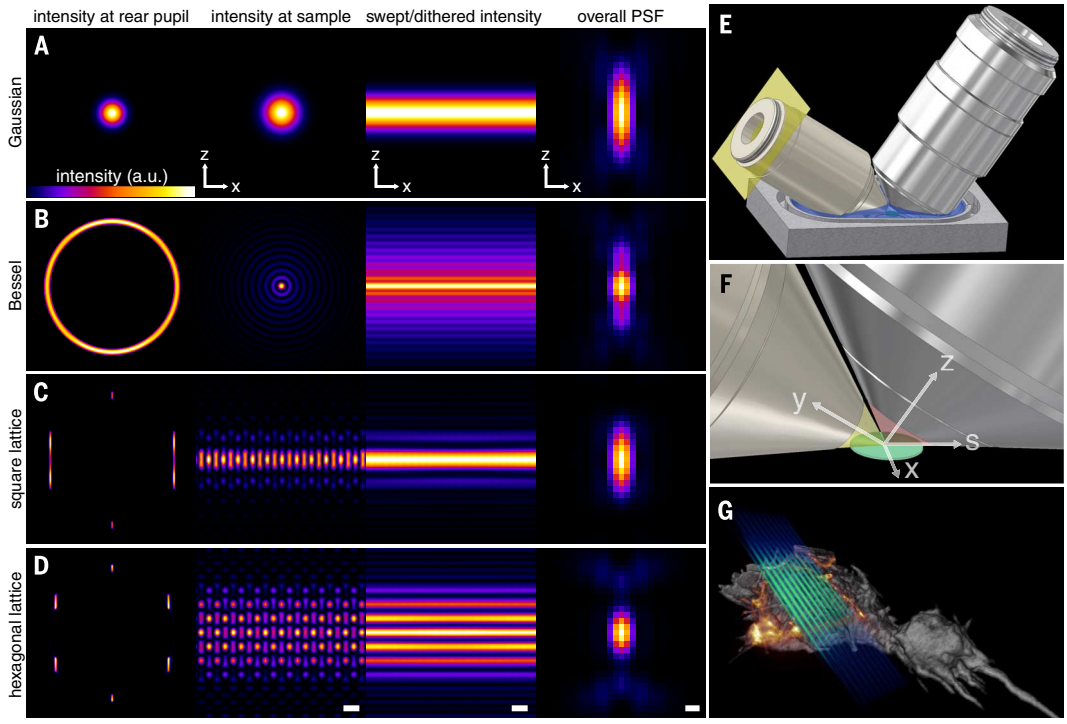

Fig. 1. Methods of light-sheet microscopy. (**A**) The traditional approach, where a Gaussian beam is swept across a plane to create the light sheet. a.u., arbitrary units. (**B**) A Bessel beam of comparable length produces a swept sheet with a much narrower core but flanked by sidebands arising from concentric side lobes of the beam. (**C** and **D**) Bound optical lattices (compare with movie S1) create periodic patterns of high modulation depth across the plane, greatly reducing the peak intensity and, as we have found, the phototoxicity in live cell imaging. The square lattice in (C) optimizes the confinement of the excitation to the central plane, and the hexagonal lattice in (D) optimizes the axial resolution as defined by the overall PSF of the microscope. The columns in (A) to (D) show the intensity pattern at the rear pupil plane of the excitation objective; the cross-sectional intensity of the pattern in the *xz* plane at the focus of the excitation objective (scale bar, 1.0 μm); the cross-sectional intensity of the light sheet created by dithering the focal pattern along the *x* axis (scale bar, 1.0 μm); and the *xz* cross section of the overall PSF of the microscope (scale bar, 200 nm). (**E**) Model showing the core of our microscope, with orthogonal excitation (left) and detection (right) objectives dipped in a media-filled bath (compare with fig. S4). (**F**) Higher magnification view, showing the excitation (yellow) and detection (red) light cones, which meet at a common focus within a specimen that is either mounted or cultured onto a cover glass within the media. The *x*, *y*, and *z* directions are indicated. The *s*-axis defines the direction the specimen moves from image plane to image plane. (**G**) Representation of a lattice light sheet (blue-green) intersecting a cell (gray) to produce fluorescence (orange) in a single plane. The cell is swept through the light sheet to generate a 3D image (compare with movie S2).

lattice light sheet as a binary phase pattern on the SLM (fig. S5). Incident laser light is then diffracted by the SLM, filtered by the mask, and focused by the excitation objective to produce a light sheet and corresponding PSFs in good agreement with theoretical predictions (fig. S6).

To apply such light sheets to in vivo imaging, the excitation objective and an orthogonal detection objective were suspended from above with their ends dipped in a shallow media-filled and temperature-controlled bath (Fig. 1E), at an angle (Fig. 1F) in the *yz* plane such that their light cones of excitation (yellow) and detection (red) lie on one side of a horizontally mounted cover slip upon which the specimen rests. The lattice light sheet created in the *xy* plane at their common foci intersects the specimen obliquely (Fig. 1G). As the specimen is moved through the light sheet, the fluorescence thereby generated is recorded as series of 2D images on a camera. These are then assembled into a 3D image, and the process is repeated to build a 4D data set of cellular dynamics.

We operated the microscope in one of two different modes: a superresolution SIM mode or a high-speed dithered mode. In the SIM mode, we recorded F images at every z plane as we stepped the lattice light sheet in the x direction in F equal fractions of the lattice period. These data were then used to reconstruct a 3D image (*9*) with resolution extended beyond the diffraction limit in x and z. In the dithered mode, we used a galvanometer (fig. S4) to oscillate the lattice pattern back and forth in x at an amplitude larger than the lattice period and a speed fast compared with the camera exposure time, providing time-averaged uniform illumination across the *xy* plane. In this mode, we needed to capture only one 2D image at each z plane, but the resolution remained diffraction-limited.

We imaged the dynamics of filopodia on HeLa cells transiently expressing mEmerald-Lifeact and found that lattice light-sheet microscopy substantially outperformed our earlier Bessel beam approach. We chose cells of similar morphology and expression level for all trials and imaged each at the same excitation power. In the SIM mode, the resolution of the two approaches (Fig. 2, A and B) and the *xz* extension beyond the diffraction limit (Fig. 2, E and F) were similar. However, in nine trials of 100 3D image volumes acquired by each approach, all cells imaged by lattice SIM exhibited minimal bleaching or changes in morphology indicative of stress, whereas all but one of the cells imaged by Bessel SIM retracted (e.g., Fig. 2B, inset), six of them within the first 50 volumes. This is likely due to the much lower intensity across the lattice light sheet, as well as the much higher signal-to-noise ratio (SNR) obtained because of its coherent modulation, versus the incoherent modulation produced with a stepped Bessel beam. In practice, this led to an ~75% reduction in the total radiation delivered and ~three times faster imaging for patterns of similar period. It also allowed us to use finer patterns (fig. S3A) that require fewer steps F per plane. As a result, over 200 3D volumes could be acquired at 4.0-s intervals by lattice SIM, 6.6 times faster than with our previous Bessel approach.

In the dithered mode, we could construct low background lattices (e.g., Fig. 1C) where nearly all the excitation is within the narrow depth of focus of a high numerical aperture ($NA_{det} = 1.1$) detection objective (fig. S7). This affords high-resolution, high-contrast 2D imaging within multicellular specimens at up to 100 frames per second for thousands of time points (movie S6). In comparison, a swept Bessel light sheet exhibited substantial out-of-focus background (Fig. 1B) over a similar field of view.

Another advantage of the dithered mode is that we can craft high-resolution lattices (e.g., Fig. 1D and fig. S2) with an even more tightly confined excitation plane, although unavoidably flanked by several progressively weaker parallel planes. However, by choosing the spacing of these planes to match the nodes of the detection PSF (fig. S7), such lattices yield 3D images of substantially higher axial resolution (Fig. 2, C and G) than can be obtained with a swept Bessel light sheet (Fig. 2, D and H). In fact, the dithered lattice resolution [as defined by the optical transfer function (OTF)] (Fig. 2G) is 230 nm in x and ~370 nm in z, assuming green fluorescent protein (GFP) excitation and emission. This is only

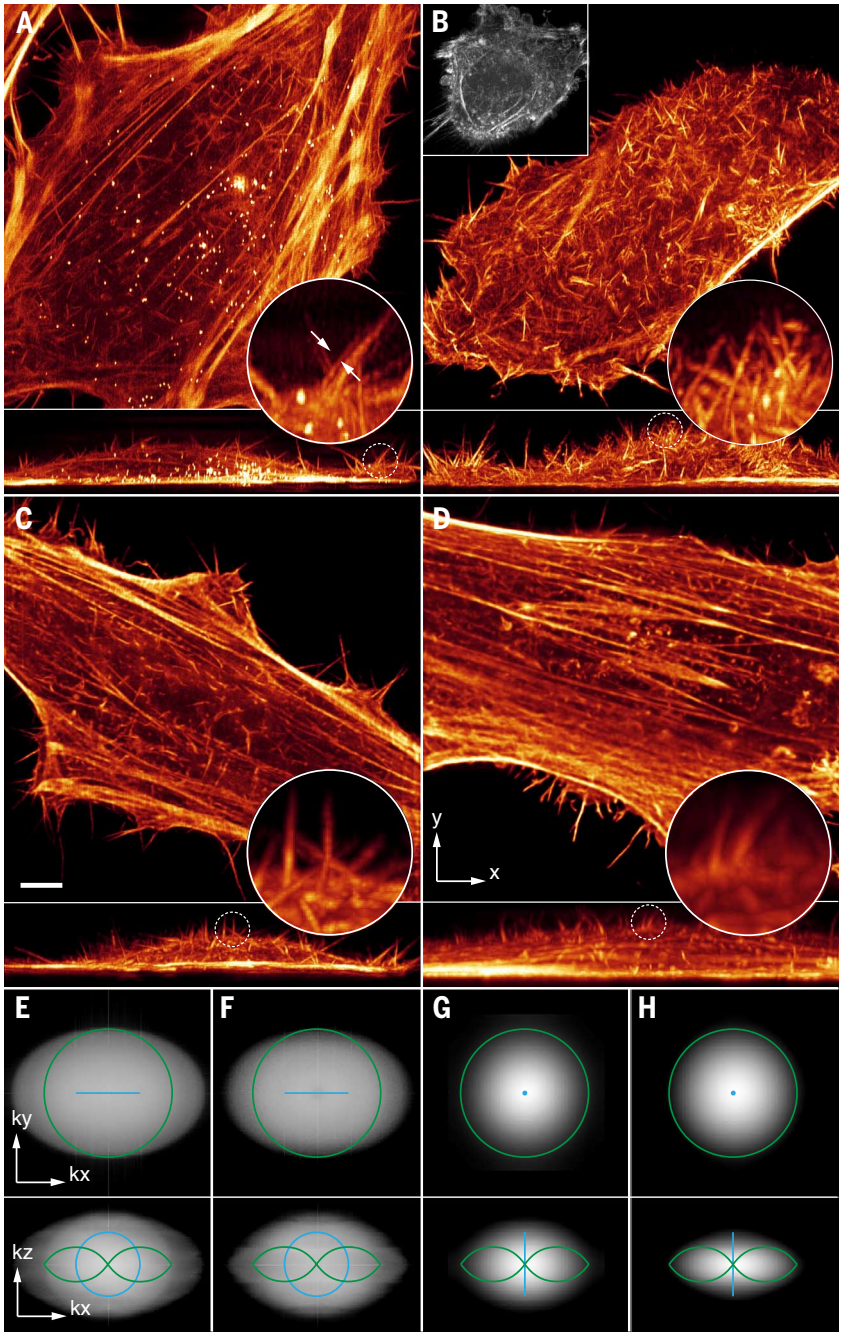

Fig. 2. Experimental comparisons of Bessel beam and lattice light-sheet microscopy. (**A**) Three-dimensional renderings in the *xy* (top) and *xz* (bottom) directions of the 300th time point of a 4D data set of a living HeLa cell transfected with mEmerald-Lifeact, taken in the SIM mode with a five-phase hexagonal lattice at 7.5-s intervals. (**B**) First time point from a different live HeLa cell imaged with a stepped Bessel beam and five-phase SIM at 30-s intervals. Square inset shows the same cell, retracted at the 32nd time point (compare with movie S3). The coherent lattice light sheet generates a pattern of much greater modulation depth (compare with movie S4), requiring less power and generating less damage to produce an image of comparable SNR. It also allows finer, three-phase patterns to be used for SIM mode imaging as fast as 4 s per volume (compare with movie S5). (**C**) The 300th time point from a third HeLa cell, acquired with a hexagonal lattice in the dithered mode at 1.5 s intervals (compare with Movie 1). Scale bar, 5 μm. The low photoxicity of this mode permits even light-sensitive specimens such as *D. discoideum* to be imaged for long periods (compare with movie S7 and Movie 3). (**D**) First time point from a fourth HeLa cell, acquired with a swept Bessel beam at 1.5-s intervals. Circular insets in (A) to (D) show magnified *xz* views of filopodia. (**E**) OTFs in log scale showing amplitudes of spatial frequencies for the hexagonal lattice SIM mode used in (A). (**F**) OTFs for the Bessel SIM mode used in (B). (**G**) OTFs for the dithered hexagonal lattice used in (C). (**H**) OTFs for the swept Bessel mode used in (D). Green curves in (E) to (H) represent the diffraction limit of the detection. Blue curves in (E) to (H) represent the diffraction limit of the excitation.

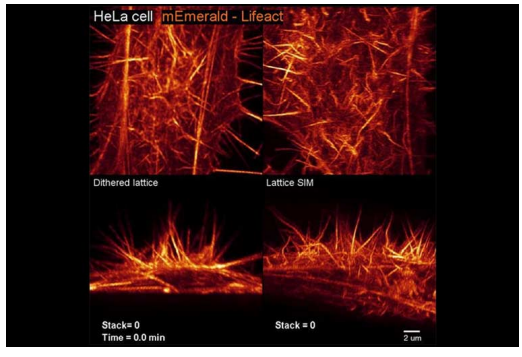

Movie 1. Top and side view volume renderings of filopodia in a HeLa cell expressing mEmerald-Lifeact. The high speed of the dithered mode of lattice light-sheet microscopy (**left**) is compared against the high resolution of the SR-SIM mode (**right**).

~1.3 to 1.5 times poorer in each direction than the 150 nm–by–280 nm *xz* resolution we obtain in the SIM mode (Fig. 2E), yet these lattices allow us to image ~7.5 times faster at comparable SNR (Movie 1). Furthermore, in the dithered mode, we can image many specimens indefinitely in 3D without photobleaching or noticeable phototoxicity. This includes even notoriously light-sensitive specimens such as *Dictyostelium discoideum*, in which we have imaged for hundreds of time points the rapid 3D dynamics of microtubules in multinucleate cells (*16*), (Movie 2, 2.0 seconds per volume); the contractile vacuole network, an extremely light-sensitive organelle composed of interconnected tubules and bladders (*17*); and filamentous cortical actin (*18*) (Movie 3, 1.0 s per volume). Thus, in practice we have found that, unless the additional resolution of the SIM mode is absolutely essential, the dithered lattice light sheet is the preferred option for most biological systems.

Single-molecule tracking and superresolution

The ability to detect and determine to nanometer precision the positions of single fluorescent molecules in vivo (*19*), either bound or diffusing, is essential to understand the molecular basis of cellular physiology. To cover cellular volumes with sufficient time resolution, widefield excitation is typically used, but the resulting out-of-focus background often limits observations to the thinner regions of single cells or confined subregions such as the plasma membrane. Light-sheet microscopy has been applied to address this issue (*20*, *21*) but with conventional Gaussian light sheets that are, over cellular dimensions, at least ~two to five times thicker than the depth of focus of a high-NA detection objective. Consequently, the majority of the illuminated molecules are still out of focus and produce large, blurred spots that cannot be localized precisely. Furthermore, very low molecular concentrations are needed to ensure that these out-of-focus spots do not overlap with the much smaller spots of in-focus molecules, compromising the localization of the latter. As a result, Gaussian light sheets substantially limit the number of molecules that can be studied per unit time and therefore the density as well as the

Corrected 30 January 2015; see full text.

precision of the localization map obtained for a given total radiation dose to the specimen.

We used dithered lattice light sheets in the low-background configuration (Fig. 1C) to overcome these problems; even over a 50-μm field of view, we can still confine the excitation to a band with a full width at half maximum (FWHM) of ~1.0 μm. This is comparable to the ~1.1-μm depth of focus of the detection objective, and thus nearly all illuminated molecules are in focus. This allowed us to study the diffusion and binding kinetics of single TMR-HaloTag (Promega)–labeled Sox2 transcription factors at high SNR not in just single isolated cells at low density (*22*, *23*) but across a densely labeled ~35-μm-diameter spheroid of mouse embryonic stem cells (Fig. 3, A and B), where epi-illumination revealed nothing and single Bessel beam plane illumination exhibited much lower SNR because of side lobe excitation. Analyzed within four nuclei (Fig. 3C), the diffusion of Sox2 fit well to a biexponential curve (Fig. 3, D and E) having a fast coefficient of 0.89 ± 0.07 $\mu m^2/s$ and a slow coefficient of 0.13 ± 0.01 $\mu m^2/s$. It had been shown previously that these two diffusion coefficients represent nonspecific and DNA-specific binding interactions (*22*). In contrast, within the cytoplasm, high-speed imaging revealed that the diffusion was 10-fold greater: 8.4 ± 0.2 $\mu m^2/s$ for a coefficient representing free diffusion or directed transport into the nucleus and 0.74 ± 0.03 $\mu m^2/s$ for a coefficient related to transient, nonspecific interactions.

Another important application of single-molecule localization is superresolution microscopy (*24*). As above, this has been most often applied to single cells in order to have sufficient SNR for precise localization, although Gaussian light sheets have also been used (*25*) to extend the approach to multicellular specimens. However, in either case, out-of-focus molecules substantially reduce the median localization precision, the localization rate, and the fraction of molecules localized rather than lost to photobleaching, which together reduce the speed and resolution of the technique. These problems are exacerbated when the method is extended to 3D, where the axial position of each molecule is inferred from the shape of its image, either directly from defocus (*26*) or with applied astigmatism (*27*). Here, even under ideal circumstances, the lateral localization precision decreases rapidly with distance from the focal plane, and minute background variations resulting from neighboring molecules can render the localization inaccurate in all three dimensions.

With a dithered lattice light sheet, on the other hand, we could extend 3D localization-based superresolution to thick specimens without sacrificing the localization precision, localization rate, or fraction of total molecules localized that is achievable in the optimal limit of a thin specimen. To demonstrate, we used photoactivated localization microscopy (PALM) (*28*) with applied astigmatism to image Dendra2–lamin A at the nuclear envelope of a fixed U2OS cell. We scanned a region around the nucleus of the cell 31,600 times through the 1.1-μm-thick light sheet in 61 steps of 0.50 μm each to ensure that every molecule would be detected at high SNR and that fluorescent bead fiducial markers would be visible across multiple steps. This allowed us to accurately assemble the narrow slab of 3D localization data from each 2D image at each sample position into a much larger 3D picture encompassing the entire field of view. At each step, we applied an 8-ms pulse of 405-nm light and then imaged the molecules thereby activated for 95 ms under 560-nm excitation.

In the end, we localized 4.2×10^6 molecules with a median emission of 645 photons to a median precision of $\sigma_x = 10.4$ nm, $\sigma_y = 8.2$ nm, and $\sigma_z = 45.4$ nm (Cramer Rao lower bound) across a volume of 51 μm by 26 μm by 30 μm. Compared with a diffraction-limited, deconvolved 3D image acquired with the dithered lattice light sheet before PALM imaging (Fig. 3F), the resulting 3D PALM image (Fig. 3, G and H) reveals far more structural detail in the nuclear envelope, such as a twisted braid of lamin A on the inner surface (Fig. 3, G and H, inset). The mean localization density within this feature is 2.2×10^4 localizations/μm^3, corresponding to a resolution limit defined by the Nyquist criterion of 71 nm. An exploded view in three sections (Fig. 3H) also reveals at high resolution envelope invaginations (*29*) that form channels spanning the entire thickness of the nucleus.

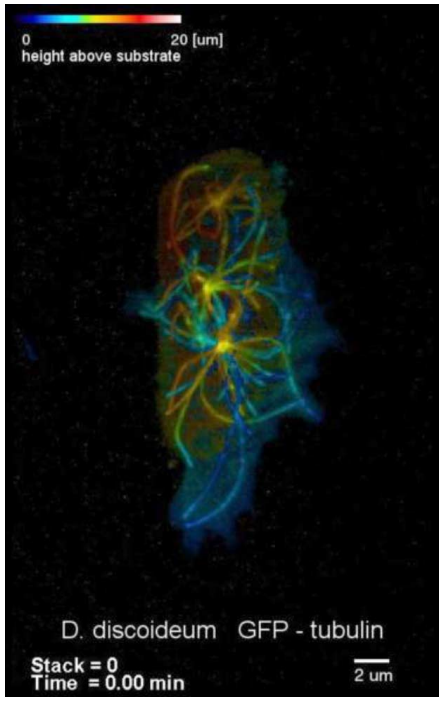

Movie 2. Top view of microtubule dynamics in multinucleate *D. discoideum* cells expressing GFP-tubulin. Cells are color-coded based on their height above the substrate, over 1430 time points at 2.0-s intervals. Rapid translational movements present in the movie represent a recentering of the organism within the microscope field of view.

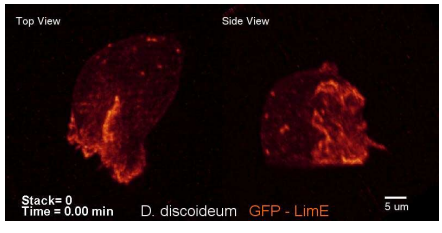

Movie 3. Top- and side-view volume renderings of actin-associated GFP-LimE in a *D. discoideum* cell. Images taken over 150 time points at 1.0-s intervals, highlighting a transient, extremely rapid "lightning bolt" of actin-rich material in the cell cortex.

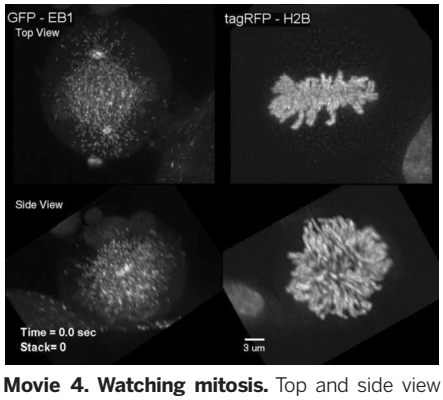

Movie 4. Watching mitosis. Top and side view maximum-intensity projections after deconvolution of GFP-EB1 at growing microtubule ends (**left**) and TagRFP-H2B highlighting chromosomes (**right**) in a HeLa cell at three different stages of mitosis.

Noninvasive 3D imaging of intracellular dynamics

The dividing cell is a spatially complex, highly dynamic environment. This is perhaps nowhere more evident than in the dynamic instability of microtubules (MTs), which undergo rapid, stochastically switched phases of growth and shrinkage during mitosis. Growing MT ends are decorated with the accessory protein EB1, which, when fluorescently labeled, provides a punctuate marker of the growing end (*30*). In interphase, it is relatively straightforward to apply 2D single-particle tracking algorithms to widefield or confocal live cell data and quantify this growth in space and time. In mitosis, however, the thickness of the cell and density and speed of these punctae (Movie 4) demand a much higher level of 4D spatiotemporal resolution to allow them to be isolated and tracked precisely. Such resolution is afforded by the dithered lattice light sheet.

To demonstrate, we imaged HeLa cells stably expressing GFP-EB1 and mTagRFP-H2B throughout mitosis, identified the stage of mitosis by the morphology of the chromosomes (from H2B), and quantified the EB1 tracks with a 2D algorithm (*31*) that we modified for 3D. From these data, we were able to extract the 3D microtubule tip positions, growth phase lifetimes, and growth velocities across the entire cell. In a typical experiment (Fig. 4A and Movie 5), we recorded ~100 two-color 3D volumes at 1.5-s intervals, waited 5 to 10 min for the cell to recover from the excitation while it advanced to a later stage, and then repeated this process through cytokinesis. Despite the extreme sensitivity of the cell during mitosis (*32*), we could often record ~500 3D volumes in each trial, yet still each cell would pass through its mitotic checkpoints and divide

normally. Quantification from 12 cells (fig. S8) revealed that microtubule (MT) growth accelerates during the early stages of mitosis, doubling velocity by prometaphase/metaphase, and then gradually decelerates until reaching the original interphase velocity distribution in cytokinesis. Although harder to quantify, 3D images also suggest a higher mean velocity for kinetochore MT growth than astral MT growth during anaphase/telophase (fig. S8 and Movie 5).

We also imaged the spatiotemporal relationship of the endoplasmic reticulum (ER), mitochondria,

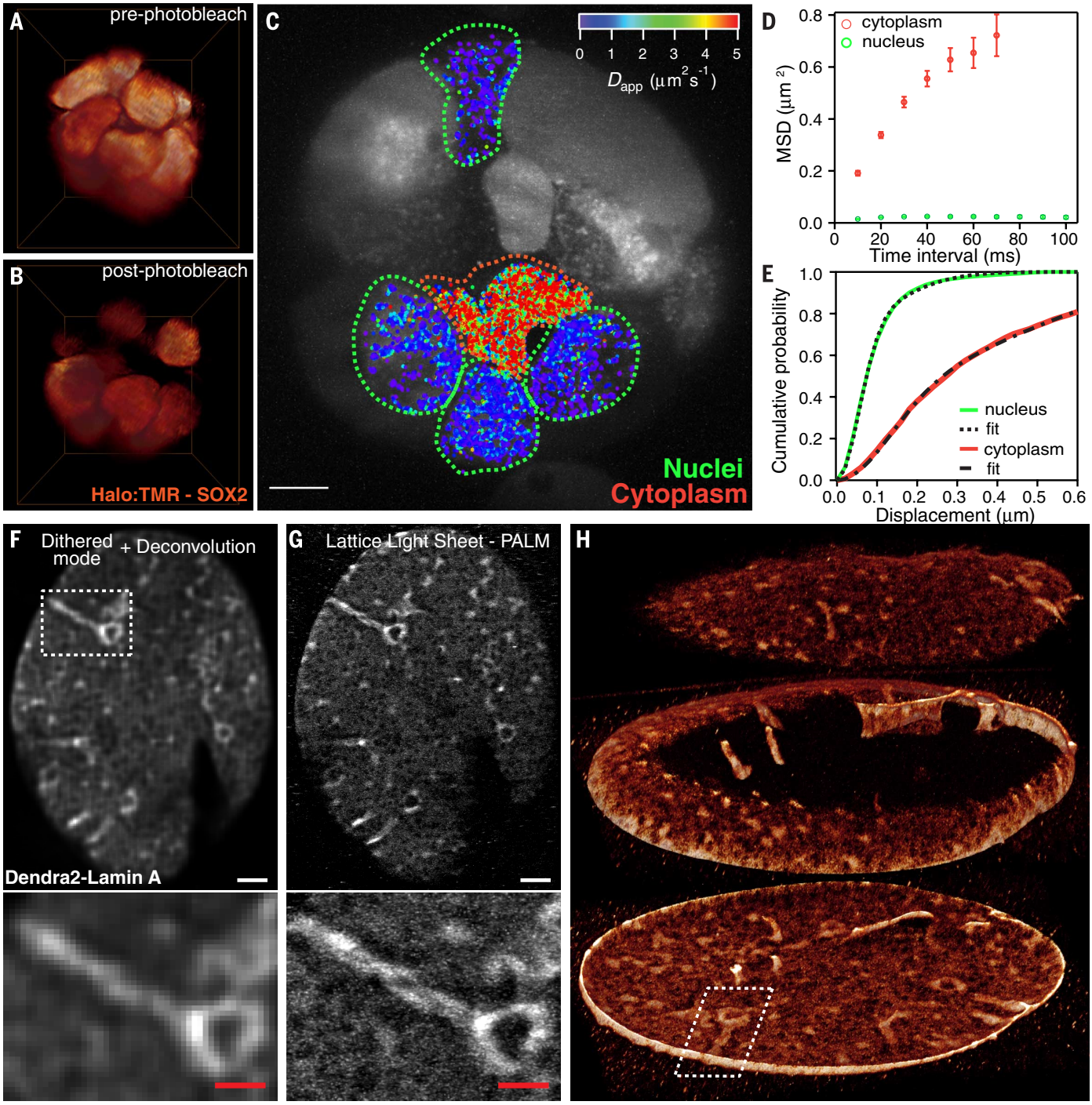

Fig. 3. Single-molecule tracking and superresolution. (**A**) Lattice light sheet 3D rendering of a ~35-μm-diameter spheroid of mouse embryonic stem cells containing TMR-labeled Sox2 transcription factors. (**B**) Same spheroid, showing bleached region after single-molecule imaging with the light sheet dithered at a fixed plane (compare with movies S8 and S9). (**C**) Local apparent diffusion coefficients of Sox2 molecules. Scale bar, 5 μm. (**D**) MSDs of molecules in the nuclei (7608 trajectories) or cytoplasm (2339 trajectories) with error bars indicating the standard errors of the means. (**E**) Corresponding cumulative distribution functions (CDFs) representing the fraction of all tracked molecules at a given MSD or below. (**F**) Diffraction-limited maximum intensity projection (MIP) from a 600-nm-thick slab cut through the bottom of the nuclear membrane of a fixed U2OS cell expressing Dendra2–lamin A, taken in the dithered lattice mode. (**G**) Super-resolution MIP from the same slab, taken with 3D PALM, where molecules in successive planes are excited with a dithered lattice light sheet. Scale bars, 2 μm in upper views of (F) and (G), 1 μm in zoomed boxes below. (**H**) Exploded view of the full 3D rendering of the nuclear envelope by PALM (compare with movie S10).

Corrected 30 January 2015; see full text.

and chromosomes during mitosis by using three-color lattice light sheet microscopy. We labeled LLC-PK1 cells stably transfected with mEmerald-ER and mApple-H2B with MitoTracker Deep Red dye (Life Technologies) and recorded 300 3D volumes in each color at 3.8-s intervals by acquiring a 2D image in each color at each z plane before moving on to the next (Fig. 4B and Movie 6). As reported elsewhere, in mitosis the mitochondria fragment (*33*) and the ER reorganizes into large, extended cisternae (*34*) with little remaining of the reticular network familiar to interphase. However, with the lattice light sheet we additionally see that the mitochondrial fragments nestle within and are corralled by the ER cisternae as they move fluidly within and between these pockets. We observed no exchange of fluorophore between mitochondria and the ER, which would be suggestive of their mutual fusion. Last, both organelles were excluded from the region occupied by the chromosomes and the mitotic spindle during anaphase/telophase.

Whereas our current system is capable of imaging at up to 200 planes per second in multiple colors and up to 1000 planes per second in a single color over a 100 μm–by–20 μm xy field of view, biological systems still exist for which even higher speed is desired. An example is the model protozoan *Tetrahymena thermophila* (*35*): We imaged a GFP-scramblase expressing specimen that was trapped in a pocket of 0.5% low melting point agarose for 1250 time points at 3.2 volumes per second (Fig. 4C and Movie 7). However, the temporal resolution was insufficient to continuously follow the rapid morphological changes that we observed or allay the fear of motion-induced artifacts. We then transitioned to 2D imaging of a single plane on the same specimen at 3 ms per frame. We were then able to smoothly track for 18,000 frames the motion of even the fastest processes falling within the image plane, such as the beating of motile cilia (fig. S10), raising the possibility of quantifying their bending and the forces they generate to elucidate their roles in signal transduction and locomotion. The combination of 3D and 2D imaging represented more than 200,000 images obtained from a single living, motile specimen within the time span of about 7.4 min. During this time, we observed no change in organism dynamics or protein distribution that would be indicative of phototoxicity.

Imaging cell-cell and cell-matrix interactions

The vast majority of cells do not live in isolation, but rather in contact with neighboring cells or an extracellular matrix (ECM). We investigated both scenarios with the dithered lattice light sheet. In one example, we imaged the initial 3D aggregation of starved *D. discoideum* cells as they rapidly chemotaxed toward one another and began the transition from unicellular to multicellular behavior (fig. S11). In another, we added a suspension of cytotoxic T cells expressing GFP-Lifeact to a field of peptide-pulsed EL4 target cells stably expressing plasma membrane markers fused to TagRFP on a cover slip and observed the processes of T cell/target cell engagement and the formation of the immunological synapse (*36*). Across dozens of trials, a stereotypic behavior emerged: A T cell, blunt at

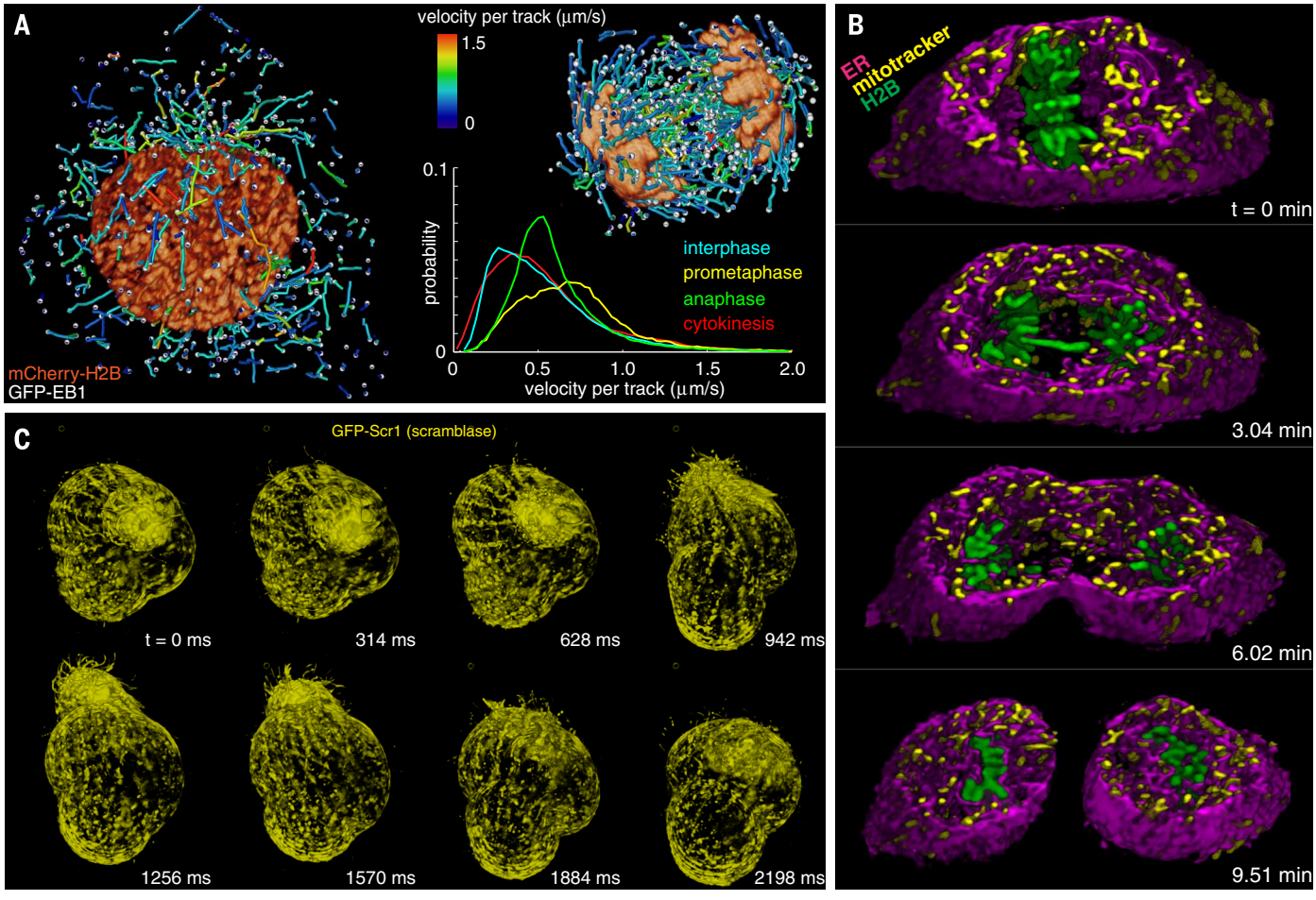

Fig. 4. Intracellular dynamics in three dimensions. (**A**) Cells in prophase (left) and anaphase (right), showing histones and 3D tracks of growing microtubule ends, color-coded by velocity. Color-coding of each track by height (movie S11) or growth-phase lifetime (movie S12) is also possible. Each image in (A) represents a distillation of a few time points from a 4D, two-color data set typically covering hundreds of time points per cell (compare with Movie 5). Graph shows the distribution of growth rates at different stages of mitosis, averaged across 9 to 12 cells (compare with figs. S8 and S9). (**B**) The 3D spatial relationship of histones (green), mitochondria (yellow), and ER (magenta) at four time points during mitosis in a slab extracted from a larger 4D, three-color data set of HeLa cells imaged for 300 time points (compare with Movie 6). (**C**) Volume renderings at eight consecutive time points of a single specimen of the protozoan *T. thermophila* taken from a 4D data set spanning 1250 time points (compare with Movie 7). Imaging at 3 ms per frame in a single plane (compare with movie S13) reveals the motions of individual cilia.

the leading end and trailing a small uropod, migrated toward a target cell while extending probing lamellipodia (Fig. 5A). Upon initial contact with the target cell, the T cell begins to establish a synapse rich in actin as the T cell rounds up (Fig. 5, B and C). Lamellipodial protrusion and movement of 3D actin structures are observed along the T cell body (Movie 8) that would be difficult to observe without the speed and resolution of the lattice microscope.

Mammalian cells typically migrate not on a 2D substrate but through a complex 3D meshwork of ECM proteins. However, because of the limitations of conventional imaging modalities, the majority of studies of cell motility have focused on the locomotion of cells on planar surfaces (*37*). Recent extensions into 3D geometries have used slowly moving mesenchymal cells such as fibroblasts (~1 μm/min) (*38*), where the speed is amenable to current technologies. However, less is known about migration of neutrophils, which must navigate at ~10-times faster speeds (~8 to 12 μm/min) (*39*) through complex 3D microenvironments in infected tissues. We studied this process by adding neutrophil-like human HL-60 cells (*40*) expressing mCherry-utrophin to a 3D, fluorescently labeled collagen mesh (Fig. 5D and Movie 9). Cells embedded in the mesh migrated at speeds comparable to cells on cover slips (Movie 10), despite the added physical constraints. They also exhibited a similar polarized morphology, with leading lamella and a trailing uropod (Fig. 5E). However, the embedded cells sent lamellar-like protrusions in a greater variety of directions as they probed alternative pathways through the mesh. We also recorded the displacement of the collagen filaments by the cells (Fig. 5F), and in the future these data might be combined with 3D traction force microscopy (*41*) to create high-spatiotemporal-resolution maps of the forces generated by the cells as they migrate through their surroundings.

Imaging the subcellular physiology of developing embryos

Much of our knowledge of cellular physiology comes from studies of immortalized cells cultured onto flat substrates. However, to understand the true physiological state of a cell, it must be studied within the multicellular environment in which it evolved. This is possible with lattice light-sheet microscopy, at least in the superficial layers of developing embryos where sample-induced aberrations are minimal. We demonstrated this in two model systems: the nematode *Caenorhabditis elegans* (Fig. 6, A and B) and the fruit fly *Drosophila melanogaster* (Fig. 6, C to F).

One challenge in such studies is that many subcellular processes occur on the time scale of seconds to minutes, whereas development from fertilization to hatching occurs over many hours to several days. However, even with the minimal invasiveness of our method, it is not possible to acquire the tens to hundreds of thousands of 3D volumes needed to follow fast subcellular dynamics over the full course of development without bleaching or damaging the specimen.

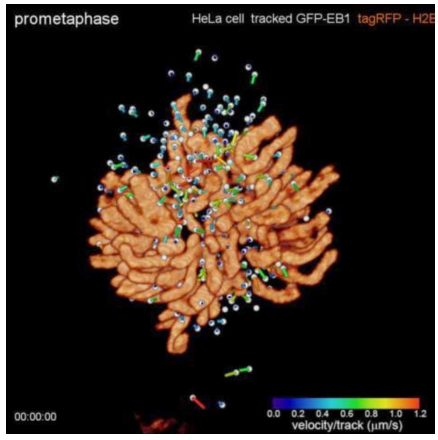

Movie 5. Measured GFP-EB1 trajectories denoting growing microtubule endpoints, color-coded by velocity, and TagRFP-H2B highlighting chromosomes, at five different stages during the division of a single HeLa cell.

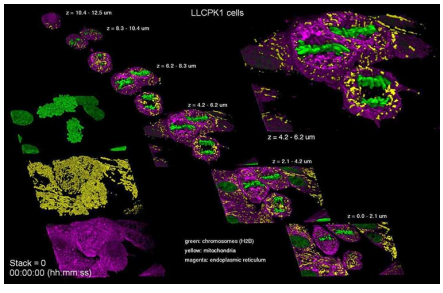

Movie 6. Chromosomes (green, mCherry-H2B), mitochondria (yellow, mitotracker–deep red), and ER (magenta, mEmerald-calnexin) in a field of dividing LLC-PK1 cells. Compare with Fig. 4B. (**Left**) Individual volume renderings. (**Center**) Three-color overlay, with the imaging volume sliced in ~2-μm-thick slabs to facilitate the visualization of the internal arrangement of the features. (**Right**) Magnified view of one such slab, showing mitochondrial fragments nestled in ER cisternae.

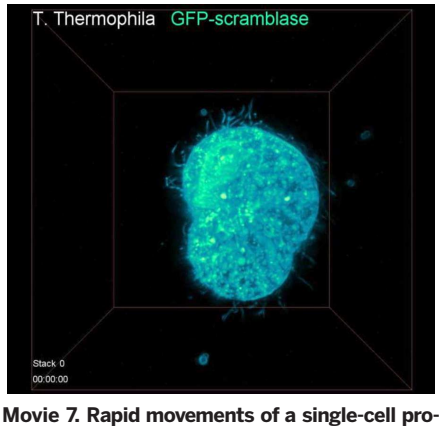

Movie 7. Rapid movements of a single-cell protozoan *T. thermophila* expressing GFP-scramblase and confined in a small pocket in agarose. Compare with Fig. 4C. Rapid translational movements present in the movie represent a recentering of the organism within the microscope field of view. Bounding box, 53 μm by 53 μm by 51 μm.

Hence, it is necessary to carefully select the exact developmental stage and imaging interval to match the process of interest at the time of interest. For example, we imaged a GFP-tagged version of the Aurora B kinase homolog AIR-2, a chromosomal passenger complex protein essential for cytokinesis in *C. elegans*, at 1-min intervals in order to follow its localization during cell division (Fig. 6A and Movie 11). As seen previously in embryos (*42*, *43*), AIR-2 localizes to metaphase chromosomes, followed by midbody microtubules in anaphase, and eventually in a persistent midbody remnant after cytokinesis. However, the thinness of our lattice light sheet allowed us to follow this process in 4D at high SNR in live embryos with remarkable detail (fig. S12). AIR-2 first associated with the chromosomes in prophase. By anaphase, it was indeed most concentrated at the spindle midzone microtubules, but some remained at the chromosomes, some at the centrosomes, and a faint residue outlined the astral microtubules. In late cytokinesis, AIR-2 was observed on the midbody remnant between the daughter cells. Although the localization of AIR-2 has been well studied in fixed samples or single 2D slices (*43*, *44*), high spatiotemporal analysis of the 3D localization of different populations of AIR-2 may provide new insight into how it regulates cell division in developing embryos.

Other dynamic processes in *C. elegans* require higher time resolution. At the threefold stage, just before hatching, muscle contractions make it difficult to follow specific features continuously over time, although we have recorded two color 3D snapshots across the entire embryo at 2.6-s intervals. At the other end of the developmental spectrum, we imaged the 3D distribution of GFP-Lifeact at 4.8-s intervals for over 300 time points from the single-cell pseudocleavage stage through the division of the AB cell in an uncompressed embryo (Fig. 6B, fig. S13, and Movie 12). We observed an initial enrichment of actin generating the pseudocleavage furrow, which progressively relaxed to create a smooth round embryo in maintenance phase. At this stage, actin became concentrated into long, bright, bundled filaments in the anterior half of the embryo. Before the formation of the first contractile ring, actin again spread across the entire embryo in dim filaments and bright punctae before becoming concentrated in the cleavage furrow during the first embryonic division. Just before the division of the AB cell, actin became enriched in the anterior portion of the P1 cell. This actin then migrated to the interface between the P1 and the ABp cells after AB division. Throughout the imaging, extremely actin-dense comets would occasionally appear and move rapidly through the cytosol. Although these comets and other stages of the cortical actin distribution have been observed previously in live embryos by spinning disk confocal microscopy (*45*), higher 4D resolution of both the actin dynamics and the shape of the embryo such as we demonstrate here will aid in developing physical models of how actomyosin forces lead to morphological changes in the early embryo (*46*), without the potential

Corrected 30 January 2015; see full text.

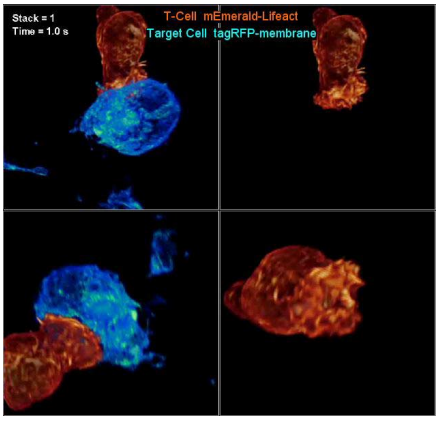

Movie 8. T cell and its target cell. Two-color volume rendering seen from two different orientations of the interaction of a T cell expressing mEmerald-Lifeact (orange) with a target cell expressing a plasma membrane marker fused to TagRFP (blue) over 430 time points at 1.3-s intervals. The target cell has been made invisible in the views in the right column (compare with Fig. 5, A to C, for a second example).

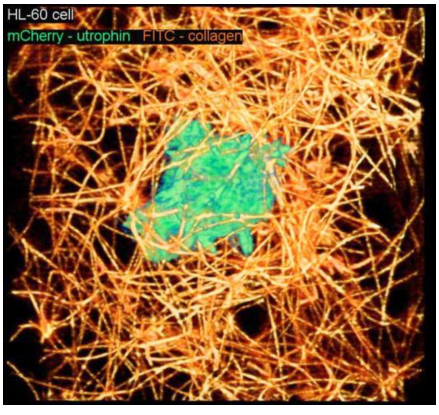

Movie 9. Cell movement through a matrix. Two-color volume rendering of a neutrophilic HL-60 cell expressing mCherry-utrophin migrating through a 3D collagen matrix labeled with FITC over 250 time points at 1.3-s intervals (compare with Fig. 5, D to F).

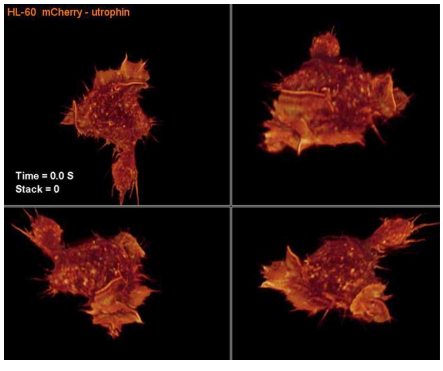

Movie 10. Cell migration in two dimensions. Volume rendering from four different viewing angles of a neurophilic HL-60 cell expressing mCherry-utrophin migrating on a 2D glass substrate over 150 time points at 1.1-s intervals.

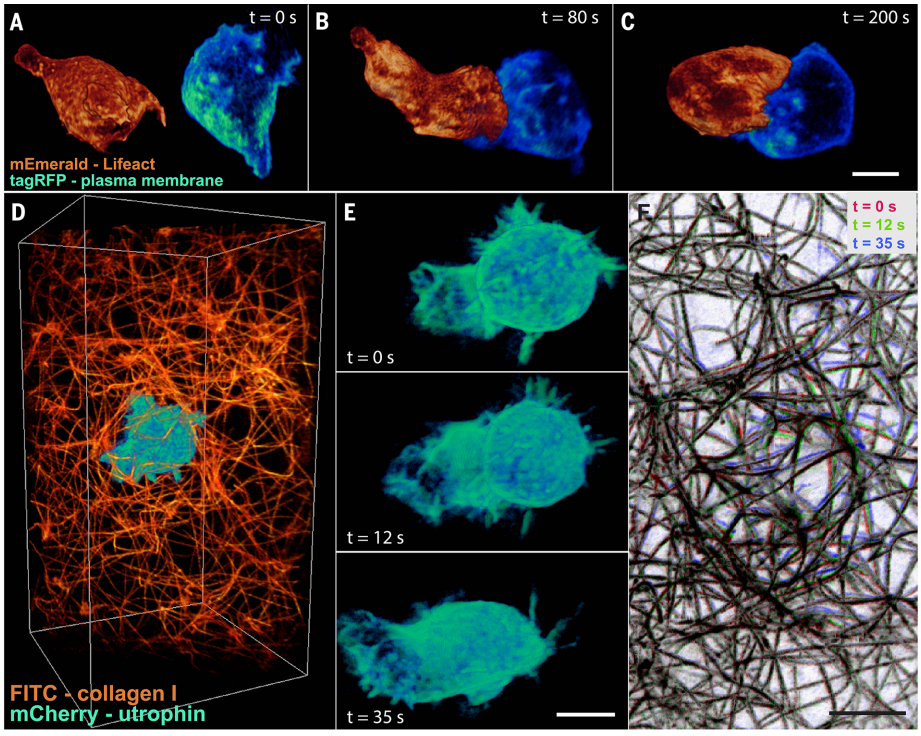

Fig. 5. Imaging cell-cell and cell-matrix interactions. (**A**) T cell expressing mEmerald-Lifeact (orange) approaching a target cell expressing a plasma membrane marker fused to TagRFP (blue), as seen from the side. (**B**) Initial contact. (**C**) The two cells, after immunological synapse formation. These data represent three time points from a 4D, two-color data set spanning 400 time points. Scale bars, 4.0 μm. Other cell-cell interactions, such as the aggregation-starved *D. discoideum* cells, can likewise be studied for extended periods (compare with movie S14). (**D**) Neutrophil-like human HL-60 cell expressing mCherry-utrophin in a fluorescently labeled collagen matrix. (**E**) Volume renderings of the cell at three time points extracted from a 4D, two-color data set of the cell and the matrix covering 250 time points (compare with Movie 9). Scale bar, 5.0 μm. (**F**) Overlaid MIPs in three different colors of the collagen at the same three time points. Colored regions highlight local displacements of the matrix by the cell. Scale bar, 5.0 μm.

artifacts introduced by the embryo compression typically applied when using spinning disk confocal microscopy.

On a larger scale, we also studied the process of dorsal closure in *D. melanogaster*, the point in embryogenesis where two lateral sheets of epithelial cells converge over an eye-shaped opening to cover the amnioserosa, a thin layer of squamous cells. In embryos expressing GFP-labeled *DE*-cadherin to mark cell boundaries, apical shape oscillations and ingression of amnioserosa cells have been previously quantified in 2D models of the curved surface extracted from 3D spinning disk data (*47*). However, with lattice light-sheet microscopy, we could study this process (Fig. 6C) in 4D up to twice as fast and at five times finer z sampling in uncompressed embryos throughout the thickness of the amnioserosa and beyond. We have also imaged embryos expressing GFP-tagged myosin (Fig. 6D and Movie 13) or sGMCA (Fig. 6E), a marker of filamentous actin at the plasma membrane, and observed contractile oscillations of the cytoskeleton temporally correlated to cell shape changes at the basal as well as the apical surface (Fig. 6F). Taken together, such data may facilitate the development of 4D models of the collective dynamics of dorsal closure as driven by forces in the amnioserosa and in the encroaching epithelium, with its actomyosin-rich purse string that resides near their mutual boundary.

Discussion

One limitation of lattice light-sheet microscopy is that, like all forms of optical microscopy, its performance degrades increasingly with depth because of sample-induced aberrations. Thus, depending on the optical heterogeneity of the specimen of interest, imaging beyond 20 to 100 μm will likely require combining the technique with adaptive optics (*48*) in both excitation and detection pathways to compensate for these aberrations.

The chief benefit of lattice light-sheet excitation for in vivo imaging is its exceptionally low photobleaching and phototoxicity—each of the 4D data sets presented here was distilled from tens to hundreds of thousands of raw 2D images acquired from each specimen. This is about an order of magnitude more images per specimen than we achieved with linear Bessel beam plane illumination (*7*, *8*) and nearly two orders of magnitude more than in typical confocal data sets of similar specimens at similar expression levels. Thus, although excitation with a line (Bessel) is better than a point (confocal), a plane (lattice) is better than a line. The implication is that, although the total light dose delivered to the

specimen is an important factor dictating its health, an even more important metric may be the peak intensity delivered to the specimen. In retrospect, this is not surprising, because photodamage mechanisms that scale supralinearly with peak intensity have been identified for both visible (*49*) and two-photon (*50*) excitation. Given that confocal and lattice light-sheet microscopy operate at similar 1- to 100-μW power levels in live cells yet distribute this power over areas that differ by 10^4 to 10^5 times in the focal plane, these mechanisms should be expected to yield vastly greater phototoxicty in the confocal case.

Indeed, seen in this context, confocal microscopy is far from an optimal tool for in vivo imaging—not only do the incoming and outgoing cones of excitation create premature bleaching and damage outside the focal plane, at the focal plane itself an actinic spot of light is created that leaves destruction in its wake as it sweeps through the specimen. Although this damage is ameliorated in spinning disk confocal microscopes that use many foci in parallel, peak intensities are still far higher than in lattice light-sheet microscopy, out-of-focus excitation remains a problem, and pinhole cross-talk can lead to artifacts and poor SNR in thick fluorescent specimens (*51*).

Another key advantage of our method is its speed. At 200 to 1000 planes per second, it is typically an order of magnitude faster than with linear Bessel beam excitation and two orders of magnitude faster than in typical spinning disk confocal systems applied to comparable specimens. This is critical, because if we wish to follow physiological processes throughout the 3D volume of the specimen with the same or better temporal resolution as in prior 2D studies, we must image at least *N*-fold faster, where *N* is the

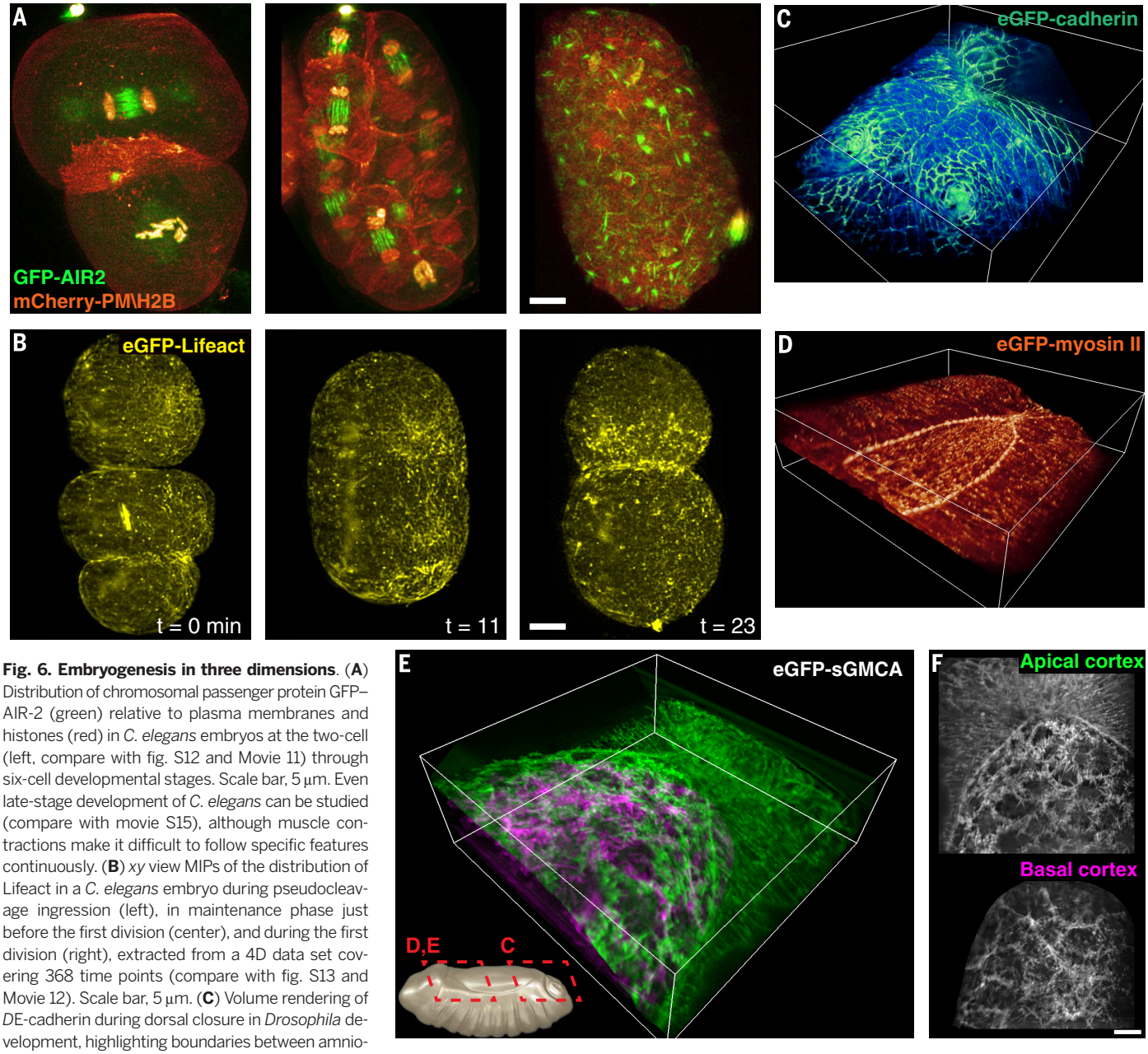

Fig. 6. Embryogenesis in three dimensions. (**A**) Distribution of chromosomal passenger protein GFP–AIR-2 (green) relative to plasma membranes and histones (red) in *C. elegans* embryos at the two-cell (left, compare with fig. S12 and Movie 11) through six-cell developmental stages. Scale bar, 5 μm. Even late-stage development of *C. elegans* can be studied (compare with movie S15), although muscle contractions make it difficult to follow specific features continuously. (**B**) *xy* view MIPs of the distribution of Lifeact in a *C. elegans* embryo during pseudocleavage ingression (left), in maintenance phase just before the first division (center), and during the first division (right), extracted from a 4D data set covering 368 time points (compare with fig. S13 and Movie 12). Scale bar, 5 μm. (**C**) Volume rendering of *D*E-cadherin during dorsal closure in *Drosophila* development, highlighting boundaries between amnioserosa cells and the formation of spiracles, from a 4D data set containing 840 time points (compare with movie S16); bounding box, 86 μm by 80 μm by 31 μm. (**D**) Myosin II during dorsal closure, highlighting the myosin-rich purse string at the interface between the outer epithelium and the amnioserosa, from a 4D data set covering 1000 time points (compare with Movie 13); bounding box, 80 μm by 80 μm by 26 μm. (**E**) sGMCA during dorsal closure, from a 4D data set covering 639 time points (compare with movie S17); bounding box, 73 μm by 73 μm by 26 μm. (**F**) MIPs highlighting cortical actin at the apical and basal surfaces of the amnioserosa, extracted from (E). Scale bar, 10 μm.

Corrected 30 January 2015; see full text.

number of 2D images comprising each 3D stack. In spinning disk confocal systems, speed limitations often make it necessary to undersample N, trading axial resolution for temporal. However, with our approach, we can image many specimens in 3D at subsecond intervals, even though $N \sim 100$ to 200 planes per time point are required by the Nyquist criterion to recover the full axial resolution of which our microscope is capable (~370 nm in the dithered mode, 280 nm in the SIM mode). Achieving such high axial and temporal resolution simultaneously (which is not possible under either the spinning disk confocal or Gaussian light-sheet paradigms) is essential: When imaging in 4D, the results are often only as strong as the weakest dimension; high-resolution information from certain dimensions is lost when smeared across the poor resolution of others.

Together, high speed and low phototoxicity position lattice light-sheet microscopy not only at the forefront of live cell fluorescence imaging but also as a key enabler to bring recent advances in biology and microscopy into mainstream application. For example, genome-edited cells (*52*) expressing endogenous levels of a targeted protein allow specimens to be studied closer to their native physiological state; however, expression levels can be far lower than in conventionally transfected specimens. This requires proportionally higher excitation intensities to yield comparable SNR at comparable speed when imaging in vivo and will severely limit their applications with conventional microscopy. High speed also expands the application space for structured illumination microscopy, which, to reconstruct artifact-free images, requires that the specimen move by less than the reconstructed voxel size in the time it takes to record the raw images contributing to that voxel. Because the elimination of out-of-focus background permits us to use shorter exposures to achieve the same SNR, we can image 3D processes that evolve at least 10 times faster by lattice light-sheet SIM than is possible with widefield SIM, albeit at somewhat lower resolution. In addition, we can image these processes far longer because of the elimination of out-of-focus photobleaching and photodamage and lower total light dose per time point. Last, for other physiological processes that evolve slowly compared with the speed of our microscope, the extra bandwidth can be expended in a fifth dimension to image in more colors. Indeed, typical cells are composed of more than 10,000 unique proteins, yet they are usually imaged in vivo only one or two at a time. By using spectral unmixing (*53*) and/or combinatorial labeling (*54*–*56*), it may prove possible with our system to study the 4D interplay of a dozen or more proteins in the same cell at the same time and to understand how they orchestrate complex cellular functions such as membrane trafficking or mitosis.

Materials and methods

Microscope optics

Seven collinear but individually modulated circular laser beams ranging in wavelength from 405 to 647 nm were passed through two pairs of cylindrical lenses to illuminate a thin stripe across the width of a ferroelectric spatial light modulator (fig. S4A, Forth Dimension Displays, SXGA-3DM). The SLM has a large number of pixels (1280 pixels by 1024 pixels) and a fast (<1 ms) switching time, the latter essential for rapid coregistered multicolor imaging. The remainder of the excitation optical path serves to create a demagnified image of the SLM (81.6-nm pixels) at the focal plane of the excitation objective, so that the pattern projected on the SLM (e.g., fig. S5C) creates a corresponding lattice light sheet of the desired properties (e.g., fig. S5G) within the specimen. First, a lens is used in a 2F configuration to create a diffraction pattern at its front focal plane (e.g., fig. S5D) that is the Fourier transform of the electric field reflected from the SLM. A custom opaque mask with transmissive annuli (e.g., fig. S5E; Photo-Sciences Incorporated) is placed at this plane, and a specific annulus is chosen to remove the unwanted diffraction orders and enforce a limit on the minimum field of view in y. The electric field transmitted through the mask (e.g., fig. S5F) is then imaged in series onto each of a pair of galvanometers (Cambridge Technology, model 6215H) and the rear pupil plane of the excitation objective. The galvanometers serve to translate the light sheet through the specimen in x and z. Last, the field is reverse-transformed by the excitation objective to create the desired lattice light sheet at its front focal plane.

The fluorescence generated within the specimen is collected by a detection objective [Nikon, CFI Apo LWD 25XW, 1.1 NA, 2-mm working distance (WD)] whose focal plane is coincident with the light sheet. Its high NA is essential to maximize the xy resolution and to optimize the light collection for single-molecule detection. The excitation objective (Special Optics, 0.65 NA, 3.74-mm WD) was custom-designed to fill the remaining available solid angle above the cover slip (Fig. 1, E and F), in order to optimize the z resolution, as well as the x resolution in the SIM mode, under this constraint.

A tube lens images the fluorescence from the illuminated slice within the specimen onto an sCMOS camera (Hamamatsu Orca Flash 4.0 v2) capable of frame rates down to 1 ms. A 3D image is produced from a stack of such 2D slices, either by moving the light sheet and detection objective together through the specimen [the former with the z galvo, the latter with a piezoelectric stage (Physik Instrumente, P-621.1CD)] or, far more commonly, by translating the specimen with a second piezo stage through the stationary light sheet along an axis s in the plane of the specimen cover slip (Fig. 1F and movie S2). The latter approach permits the use of more tightly confined light sheets for specimens that are thinner than they are long, such as single cultured cells. The specimen holder and specimen piezo are mounted on a trio of closed-loop micropositioning stages (Physik Instrumente M-663 for horizontal motion in the cover slip plane, M-122.2DD for vertical travel). In conjunction with an epifluorescence view-finding objective from below (fig. S4A, Olympus LUMPLFLN40XW, 0.8 NA, 3.3-mm WD), these are used to position the desired region of interest within the field of view of the

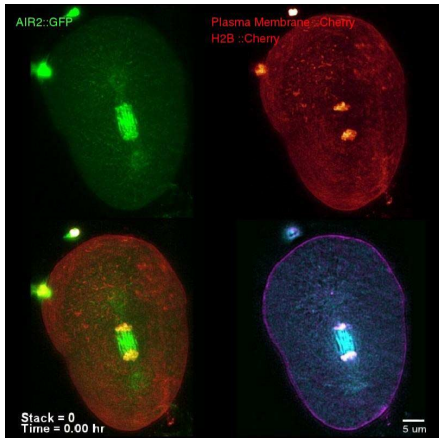

Movie 11. Protein localization in early embryo. Localization of the chromosomal passenger protein AIR-2 during the first few cell divisions of the early *C. elegans* embryo (compare with Fig. 6A and fig. S12).

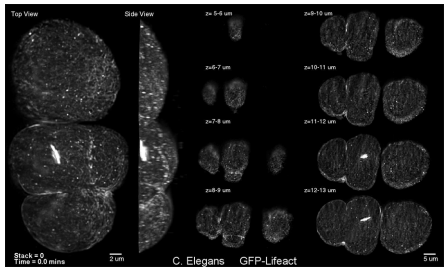

Movie 12. Actin distribution in early embryo. Various maximum intensity projections of the distribution of actin in the upper longitudinal half of a *C. elegans* embryo expressing GFP-Lifeact over 360 time points at 4.8-s intervals, from a few minutes after fertilization to just after the division of the AB cell. Left, top view. Middle, side view. Right, MIPs in eight consecutive longitudinal slabs through the data set, designed to help distinguish cortical from cytosolic actin (compare with Fig. 6B and fig. S13).

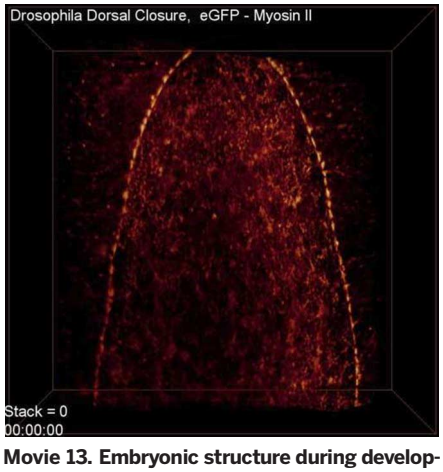

Movie 13. Embryonic structure during development. Volume rendering and orthoslices of myosin II highlighting the myosin-rich purse string during dorsal closure in a *D. melanogaster* embryo, over 1000 time points at 6.0-s intervals (compare with Fig. 6D). Bounding box, 80 μm by 80 μm by 26 μm.

light sheet. They also permit larger fields of view to be tiled together from multiple image subvolumes or multiple specimens to be imaged on the same cover slip in a repetitive loop for those cases where the dynamics occur on a time scale slow compared with the 3D imaging speed.

Complete details regarding the optical design are given in supplementary note 3. Certain aspects of the design are derived from our earlier Bessel beam work, so these earlier publications (*7*, *8*, *57*) remain valuable resources as well.

Control electronics

All analog/digital input/output signals are calculated and controlled by custom LabVIEW software (Coleman Technologies, Incorporated, National Instruments) and a field-programmable gate array card (FPGA, fig. S14, National Instruments, PCIe-7852R Virtex-5 LX50 R series). Analog outputs (AOs) controlling galvos and piezos were conditioned by individual scaling amplifiers (SRS, SIM983, and SIM900 mainframe) to match their 16-bit resolution to the control range of each device. Instrument control and data analysis were performed on independent Supermicro workstations (Supermicro X8DTG-QF) running Windows 7 Professional 64 bit (Microsoft), each equipped with two Intel Hexa-CoreXeon X5680 processors, 96 GB of RAM, and an NVIDIA GeForce GTX TITAN graphics card.

The SLM runs under internal timing and serves as the master clock for image acquisition. A series of SLM images known as a Running Order (fig. S15) is loaded into the SLM, and a hardware start signal from the FPGA triggers execution of the Running Order (fig. S16). A digital LED Enable output from the SLM is read by the FPGA and mirrored as an output sent to the scientific complementary metal-oxide semiconductor (sCMOS) camera (which operates in external trigger, rolling shutter mode), in order to synchronize the image acquisition to the positive/negative display states of the SLM (fig. S17). The number of transitions of LED Enable is counted to determine which SLM image in the Running Order is currently displayed, so the FPGA can send the appropriate outputs to control the acousto-optic tunable filter (AOTF), galvos, and piezos (fig. S18). The acceleration and flyback speeds of the latter two can be adjusted independently (fig. S19) to match their intrinsic response times. Control sequences exist to run the microscope in single or multiple colors in any one of four versions: objective scan, dithered mode (fig. S20); objective scan, SIM mode (fig. S21); sample scan, dithered mode (fig. S22); or sample scan, SIM mode (fig. S23). More complete details can be found in supplementary note 4.

Sample preparation and imaging conditions

Specimens are cultured or mounted on 5-mm-diameter cover slips (Warner Instruments, 64-0700) cleaned before use according to our earlier protocol (*7*). The cover slip is clipped to the end of a long extension of the sample holder (orange, fig. S4D). This end is dipped in a shallow media-filled bath (translucent yellow, fig. S4D), while the opposite end is bolted to the sample piezo. The bath has inlet and output ports for perfusion of the media. A subassembly with the excitation and detection objectives and their translation stages is lowered from above until the ends of the objectives are dipped in the media at the distance from the cover slip appropriate for creating a lattice light sheet near its upper surface.

For operation away from room temperature (particularly for live mammalian cells at 37°C), heated or chilled water from a remote temperature-controlled reservoir is pumped through self-contained channels cut in the base of the bath, unconnected to the bowl that contains the imaging media. Asymmetric heating or cooling of the ends of the objectives creates substantial optical aberrations that affect the microscope performance, as does convection of the media because of temperature gradients in the bath. Thus, additional heating/cooling blocks (translucent green and red, fig. S4D) with self-contained water channels are bolted around and close to the objectives, but not in contact. These are supplied with water from a second reservoir to maintain a circularly symmetric, uniform temperature around the objectives that matches the temperature of the bath. The temperatures of the two reservoirs needed to attain a given specimen temperature differ but can be determined empirically.

Preparation conditions specific to each specimen are given in the supplementary note 5. Imaging conditions specific to each specimen, including maximum and minimum excitation NA, excitation power, imaging time, image and voxel sizes, imaging mode, fluorophores, and proteins, etc., are given in table S1.

Image processing and visualization

Unless otherwise noted, all data acquired in the dithered mode were deconvolved by using a Richardson-Lucy algorithm adapted to run on a graphics processing unit (GPU) (NVIDIA, GeForce GTX TITAN), using an experimentally measured PSF for each emission wavelength. All data acquired in the SIM mode were reconstructed with an implementation of the algorithm for 3D-SIM (*9*) previously adapted for Bessel beam–structured plane illumination microscopy (*8*, *57*), running on the same GPU, using an OTF calculated from an experimentally measured PSF for each emission wavelength. All 3D data sets acquired via sample scan in the x, y, and s coordinated system were transformed ("deskewed") to the more conventional x, y, and z coordinates in the GPU before visualization. Where noted (table S1), data sets were corrected for photobleaching and hot pixels by using either built-in Image J functions (histogram matching or exponential fitting) or by rescaling the maximum display value such that about 0.1% of all voxels (99.9th percentile) at any given time point were saturated. Last, processed data sets were imported into Amira (FEI) for 5D volumetric rendering.

Single-molecule tracking and 3D PALM imaging

Single-molecule tracking within mouse embryonic stem cell spheroids (Fig. 3, A to E, and movies S8 and S9) was performed by using the particle-tracking software Diatrack (v3.03, Semasopht) as described previously (*58*). Briefly, the software fits intensity spots with fixed-width symmetric 2D Gaussian functions. A map of local apparent diffusion coefficients was generated with code written in Igor 6.3.4 (WaveMetrics). The local apparent diffusion coefficients were evaluated in 40 nm–by–40 nm grids and calculated from the mean square displacements originating from within a radius of 150 nm of each grid point over a time scale of 10 ms (Fig. 3C). The single-molecule trajectories were further analyzed by calculating mean square displacements (MSDs) for all possible time intervals and cumulative distribution functions (CDFs) of all 10-ms displacements in the sample plane (Fig. 3, D and E). The fit data from each CDF were best fit by a linear combination of two exponential functions, $P(r) = 1-[\exp(-r^2)/4D_{app}\Delta t]$, where D_{app} is the apparent diffusion coefficient and t is time, corresponding to both fast and slow components.

PALM was performed with a cylindrical lens of 1000-mm focal length (Thorlabs, LJ1516RM-A) placed 40 mm before the imaging camera, to enable axial localization via the resulting astigmatism (*27*). The sample was scanned 31,000 times in 61 steps of 500 nm each (270 nm in the z direction), for a total of 1.83×10^6 raw 2D single-molecule images. For each such image, single molecules were identified and localized in 3D by using a custom-written maximum likelihood estimator algorithm, an experimentally measured calibration curve (for z-axis fitting), and a Levenberg-Marquardt optimization. Each 3D fit was offset by the sample-piezo position at the time of acquisition and assembled into a composite 3D image. Because a molecule could be localized at multiple image planes and across multiple image volumes, an algorithm was used to link repeated localizations of the same molecule, as determined by a minimum spatial/temporal separation, into a single higher-precision localization event in the final reconstructed image. The initial localization, fit refinement, and linking were implemented on a GPU by using custom-written Matlab and CUDA code (NVIDIA). For visualization of the final data set, a 3D Gaussian with standard deviations determined by the 3D localization precision was plotted at the centroid of each localization. The voxel size of the final reconstructed image (Fig. 3, G and H, and movie S10) was 10 nm by 10 nm by 20 nm.

Tracking plus ends of microtubules during mitosis

Microtubule trajectories and velocities (Fig. 4A, Movie 5, figs. S8 and S9, and movies S11 and S12) were determined from the centroids of EB1 spots in each 3D data set by using a watershed algorithm and linked between time points using a version of plusTipTracker (*31*) that was custom-modified to accept our 4D data sets. The computed trajectories were then imported into Amira and color-coded by track velocity using the Spatial Graph data class.

Corrected 30 January 2015; see full text.

REFERENCES AND NOTES

1. D. B. Murphy, M. W. Davidson, *Fundamentals of Light Microscopy and Electronic Imaging* (Wiley-Blackwell, Hoboken, NJ, ed. 2, 2013).
2. D. J. Stephens, V. J. Allan, Light microscopy techniques for live cell imaging. *Science* **300**, 82–86 (2003). doi: 10.1126/science.1082160; pmid: 12677057
3. J. Huisken, D. Y. Stainier, Selective plane illumination microscopy techniques in developmental biology. *Development* **136**, 1963–1975 (2009). doi: 10.1242/dev.022426; pmid: 19465594
4. J. Huisken, J. Swoger, F. Del Bene, J. Wittbrodt, E. H. Stelzer, Optical sectioning deep inside live embryos by selective plane illumination microscopy. *Science* **305**, 1007–1009 (2004). doi: 10.1126/science.1100035; pmid: 15310904
5. U. Krzic, S. Gunther, T. E. Saunders, S. J. Streichan, L. Hufnagel, Multiview light-sheet microscope for rapid in toto imaging. *Nat. Methods* **9**, 730–733 (2012). doi: 10.1038/nmeth.2064; pmid: 22660739
6. R. Tomer, K. Khairy, F. Amat, P. J. Keller, Quantitative high-speed imaging of entire developing embryos with simultaneous multiview light-sheet microscopy. *Nat. Methods* **9**, 755–763 (2012). doi: 10.1038/nmeth.2062; pmid: 22660741
7. T. A. Planchon *et al*., Rapid three-dimensional isotropic imaging of living cells using Bessel beam plane illumination. *Nat. Methods* **8**, 417–423 (2011). doi: 10.1038/nmeth.1586; pmid: 21378978
8. L. Gao *et al*., Noninvasive imaging beyond the diffraction limit of 3D dynamics in thickly fluorescent specimens. *Cell* **151**, 1370–1385 (2012). doi: 10.1016/j.cell.2012.10.008; pmid: 23217717
9. M. G. Gustafsson *et al*., Three-dimensional resolution doubling in wide-field fluorescence microscopy by structured illumination. *Biophys. J.* **94**, 4957–4970 (2008). doi: 10.1529/biophysj.107.120345; pmid: 18326650
10. R. Gräf, J. Rietdorf, T. Zimmermann, Live cell spinning disk microscopy. *Adv. Biochem. Eng. Biotechnol.* **95**, 57–75 (2005). doi: 10.1007/b102210; pmid: 16080265
11. E. Betzig, Sparse and composite coherent lattices. *Phys. Rev. A* **71**, 063406 (2005). doi: 10.1103/PhysRevA.71.063406
12. K. I. Petsas, A. B. Coates, G. Grynberg, Crystallography of optical lattices. *Phys. Rev. A* **50**, 5173–5189 (1994). doi: 10.1103/PhysRevA.50.5173; pmid: 9911519
13. I. Bloch, Ultracold quantum gases in optical lattices. *Nat. Phys.* **1**, 23–30 (2005). doi: 10.1038/nphys138
14. M. Campbell, D. N. Sharp, M. T. Harrison, R. G. Denning, A. J. Turberfield, Fabrication of photonic crystals for the visible spectrum by holographic lithography. *Nature* **404**, 53–56 (2000). doi: 10.1038/35003523; pmid: 10716437
15. E. Betzig, Excitation strategies for optical lattice microscopy. *Opt. Express* **13**, 3021–3036 (2005). doi: 10.1364/OPEX.13.003021; pmid: 19495199
16. I. Tikhonenko, D. K. Nag, D. N. Robinson, M. P. Koonce, Microtubule-nucleus interactions in *Dictyostelium discoideum* mediated by central motor kinesins. *Eukaryot. Cell* **8**, 723–731 (2009). doi: 10.1128/EC.00018-09; pmid: 19286984
17. G. Jung, M. A. Titus, J. A. Hammer 3rd, The *Dictyostelium* type V myosin MyoJ is responsible for the cortical association and motility of contractile vacuole membranes. *J. Cell Biol.* **186**, 555–570 (2009). doi: 10.1083/jcb.200810147; pmid: 19687255
18. S. Diez, G. Gerisch, K. Anderson, A. Müller-Taubenberger, T. Bretschneider, Subsecond reorganization of the actin network in cell motility and chemotaxis. *Proc. Natl. Acad. Sci. U.S.A.* **102**, 7601–7606 (2005). doi: 10.1073/pnas.0408546102; pmid: 15894626
19. M. Coelho, N. Maghelli, I. M. Tolić-Nørrelykke, Single-molecule imaging in vivo: The dancing building blocks of the cell. *Integr. Biol.* **5**, 748–758 (2013). doi: 10.1039/c3ib40018b; pmid: 23525260
20. J. G. Ritter, R. Veith, J. P. Siebrasse, U. Kubitscheck, High-contrast single-particle tracking by selective focal plane illumination microscopy. *Opt. Express* **16**, 7142–7152 (2008). doi: 10.1364/OE.16.007142; pmid: 18545417
21. M. Tokunaga, N. Imamoto, K. Sakata-Sogawa, Highly inclined thin illumination enables clear single-molecule imaging in cells. *Nat. Methods* **5**, 159–161 (2008). doi: 10.1038/nmeth1171; pmid: 18176568
22. J. Chen *et al*., Single-molecule dynamics of enhanceosome assembly in embryonic stem cells. *Cell* **156**, 1274–1285 (2014). doi: 10.1016/j.cell.2014.01.062; pmid: 24630727
23. J. C. Gebhardt *et al*., Single-molecule imaging of transcription factor binding to DNA in live mammalian cells. *Nat. Methods* **10**, 421–426 (2013). doi: 10.1038/nmeth.2411; pmid: 23524394
24. E. Betzig, Proposed method for molecular optical imaging. *Opt. Lett.* **20**, 237–239 (1995). doi: 10.1364/OL.20.000237; pmid: 19859146
25. F. Cella Zanacchi *et al*., Live-cell 3D super-resolution imaging in thick biological samples. *Nat. Methods* **8**, 1047–1049 (2011). doi: 10.1038/nmeth.1744; pmid: 21983925
26. M. Speidel, A. Jonás, E. L. Florin, Three-dimensional tracking of fluorescent nanoparticles with subnanometer precision by use of off-focus imaging. *Opt. Lett.* **28**, 69–71 (2003). doi: 10.1364/OL.28.000069; pmid: 12656488
27. H. P. Kao, A. S. Verkman, Tracking of single fluorescent particles in three dimensions: Use of cylindrical optics to encode particle position. *Biophys. J.* **67**, 1291–1300 (1994). doi: 10.1016/S0006-3495(94)80601-0; pmid: 7811944
28. E. Betzig *et al*., Imaging intracellular fluorescent proteins at nanometer resolution. *Science* **313**, 1642–1645 (2006). doi: 10.1126/science.1127344; pmid: 16902090
29. J. Ellenberg *et al*., Nuclear membrane dynamics and reassembly in living cells: Targeting of an inner nuclear membrane protein in interphase and mitosis. *J. Cell Biol.* **138**, 1193–1206 (1997). doi: 10.1083/jcb.138.6.1193; pmid: 9298976
30. Y. Mimori-Kiyosue, N. Shiina, S. Tsukita, The dynamic behavior of the APC-binding protein EB1 on the distal ends of microtubules. *Curr. Biol.* **10**, 865–868 (2000). doi: 10.1016/S0960-9822(00)00600-X; pmid: 10899006
31. K. T. Applegate *et al*., plusTipTracker: Quantitative image analysis software for the measurement of microtubule dynamics. *J. Struct. Biol.* **176**, 168–184 (2011). doi: 10.1016/j.jsb.2011.07.009; pmid: 21821130
32. A. Khodjakov, C. L. Rieder, Imaging the division process in living tissue culture cells. *Methods* **38**, 2–16 (2006). doi: 10.1016/j.ymeth.2005.07.007; pmid: 16343936
33. N. Taguchi, N. Ishihara, A. Jofuku, T. Oka, K. Mihara, Mitotic phosphorylation of dynamin-related GTPase Drp1 participates in mitochondrial fission. *J. Biol. Chem.* **282**, 11521–11529 (2007). doi: 10.1074/jbc.M607279200; pmid: 17301055
34. L. Lu, M. S. Ladinsky, T. Kirchhausen, Cisternal organization of the endoplasmic reticulum during mitosis. *Mol. Biol. Cell* **20**, 3471–3480 (2009). doi: 10.1091/mbc.E09-04-0327; pmid: 19494040
35. D. Wloga, J. Frankel, From molecules to morphology: Cellular organization of *Tetrahymena thermophila*. *Methods Cell Biol.* **109**, 83–140 (2012). doi: 10.1016/B978-0-12-385967-9.00005-0; pmid: 22444144
36. A. T. Ritter, K. L. Angus, G. M. Griffiths, The role of the cytoskeleton at the immunological synapse. *Immunological Reviews* **256**, 107–117 (2013). doi: 10.1111/imr.12117; pmid: 24117816
37. D. Dormann, C. J. Weijer, Imaging of cell migration. *EMBO J.* **25**, 3480–3493 (2006). doi: 10.1038/sj.emboj.7601227; pmid: 16900100
38. P. H. Wu, A. Giri, S. X. Sun, D. Wirtz, Three-dimensional cell migration does not follow a random walk. *Proc. Natl. Acad. Sci. U.S.A.* **111**, 3949–3954 (2014). doi: 10.1073/pnas.1318967111; pmid: 24594603
39. P. Friedl, S. Borgmann, E. B. Bröcker, Amoeboid leukocyte crawling through extracellular matrix: Lessons from the *Dictyostelium* paradigm of cell movement. *J. Leukoc. Biol.* **70**, 491–509 (2001). pmid: 11590185
40. A. B. Hauert, S. Martinelli, C. Marone, V. Niggli, Differentiated HL-60 cells are a valid model system for the analysis of human neutrophil migration and chemotaxis. *Int. J. Biochem. Cell Biol.* **34**, 838–854 (2002). doi: 10.1016/S1357-2725(02)00010-9; pmid: 11950599
41. W. R. Legant *et al*., Measurement of mechanical tractions exerted by cells in three-dimensional matrices. *Nat. Methods* **7**, 969–971 (2010). doi: 10.1038/nmeth.1531; pmid: 21076420
42. J. N. Bembenek, K. J. Verbrugghe, J. Khanikar, G. Csankovszki, R. C. Chan, Condensin and the spindle midzone prevent cytokinesis failure induced by chromatin bridges in *C. elegans* embryos. *Curr. Biol.* **23**, 937–946 (2013). doi: 10.1016/j.cub.2013.04.028; pmid: 23684975
43. J. M. Schumacher, A. Golden, P. J. Donovan, AIR-2: An Aurora/Ipl1-related protein kinase associated with chromosomes and midbody microtubules is required for polar body extrusion and cytokinesis in *Caenorhabditis elegans* embryos. *J. Cell Biol.* **143**, 1635–1646 (1998). doi: 10.1083/jcb.143.6.1635; pmid: 9852156
44. M. Carmena, W. C. Earnshaw, The cellular geography of aurora kinases. *Nat. Rev. Mol. Cell Biol.* **4**, 842–854 (2003). doi: 10.1038/nrm1245; pmid: 14625535
45. N. Velarde, K. C. Gunsalus, F. Piano, Diverse roles of actin in *C. elegans* early embryogenesis. *BMC Dev. Biol.* **7**, 142 (2007). doi: 10.1186/1471-213X-7-142; pmid: 18157918
46. S. W. Grill, Growing up is stressful: Biophysical laws of morphogenesis. *Curr. Opin. Genet. Dev.* **21**, 647–652 (2011). doi: 10.1016/j.gde.2011.09.005; pmid: 21982413
47. A. Sokolow, Y. Toyama, D. P. Kiehart, G. S. Edwards, Cell ingression and apical shape oscillations during dorsal closure in *Drosophila*. *Biophys. J.* **102**, 969–979 (2012). doi: 10.1016/j.bpj.2012.01.027; pmid: 22404919
48. K. Wang *et al*., Rapid adaptive optical recovery of optimal resolution over large volumes. *Nat. Methods* **11**, 625–628 (2014). doi: 10.1038/nmeth.2925; pmid: 24727653
49. G. Donnert, C. Eggeling, S. W. Hell, Major signal increase in fluorescence microscopy through dark-state relaxation. *Nat. Methods* **4**, 81–86 (2007). doi: 10.1038/nmeth986; pmid: 17179937
50. N. Ji, J. C. Magee, E. Betzig, High-speed, low-photodamage nonlinear imaging using passive pulse splitters. *Nat. Methods* **5**, 197–202 (2008). doi: 10.1038/nmeth.1175; pmid: 18204458
51. T. Shimozawa *et al*., Improving spinning disk confocal microscopy by preventing pinhole cross-talk for intravital imaging. *Proc. Natl. Acad. Sci. U.S.A.* **110**, 3399–3404 (2013). doi: 10.1073/pnas.1216696110; pmid: 23401517
52. J. D. Sander, J. K. Joung, CRISPR-Cas systems for editing, regulating and targeting genomes. *Nat. Biotechnol.* **32**, 347–355 (2014). doi: 10.1038/nbt.2842; pmid: 24584096
53. T. Zimmermann, J. Rietdorf, R. Pepperkok, Spectral imaging and its applications in live cell microscopy. *FEBS Lett.* **546**, 87–92 (2003). doi: 10.1016/S0014-5793(03)00521-0; pmid: 12829241
54. J. Livet *et al*., Transgenic strategies for combinatorial expression of fluorescent proteins in the nervous system. *Nature* **450**, 56–62 (2007). doi: 10.1038/nature06293; pmid: 17972876
55. E. Lubeck, L. Cai, Single-cell systems biology by super-resolution imaging and combinatorial labeling. *Nat. Methods* **9**, 743–748 (2012). doi: 10.1038/nmeth.2069; pmid: 22660740
56. A. M. Valm *et al*., Systems-level analysis of microbial community organization through combinatorial labeling and spectral imaging. *Proc. Natl. Acad. Sci. U.S.A.* **108**, 4152–4157 (2011). doi: 10.1073/pnas.1101134108; pmid: 21325608
57. L. Gao, L. Shao, B. C. Chen, E. Betzig, 3D live fluorescence imaging of cellular dynamics using Bessel beam plane illumination microscopy. *Nat. Protoc.* **9**, 1083–1101 (2014). doi: 10.1038/nprot.2014.087; pmid: 24722406
58. B. P. English *et al*., Single-molecule investigations of the stringent response machinery in living bacterial cells. *Proc. Natl. Acad. Sci. U.S.A.* **108**, E365–E373 (2011). doi: 10.1073/pnas.1102255108; pmid: 21730169

ACKNOWLEDGMENTS

We thank L. Gao, now at Stony Brook University, for technical expertise; the Shared Resource teams at Janelia for their skill and dedication in specimen handling and preparation; and the Instrument Design and Fabrication team for their manufacturing expertise. B.-C.C., W.R.L., K.W., L.S., Z.L., B.P.E., and E.B. are funded by the Howard Hughes Medical Institute (HHMI). We also gratefully acknowledge the support of the Janelia Visitor Program. C.J. is supported by NIH grant R01GM080370. X.S.W. and J.A.H. are funded by the Division of Intramural Research, National Heart, Lung, and Blood Institute, NIH. Y.M.-K. is supported by the Japan Society for the Promotion of Science–NEXT program LS128, the Uehara Memorial Foundation, the Takeda Science Foundation, the Kurata Memorial Hitachi Science and Technology Foundation, and an intramural grant from the RIKEN Center for Developmental Biology. A.T.R. and J.L.S. acknowledge G. M. Griffiths of the University of Cambridge as the doctoral cosupervisor of A.T.R., who provided technical expertise with CTL experiments. These experiments are a collaboration with GMG. L.F.L. and R.D.M. were supported by NIH grant RM01-GM61010 and HHMI. A.-C.R. is supported by the Human Frontier Science Program LT000926/2012. S.W.G. acknowledges support from the European Research Council starting grant 281903. J.T.W. and G.S. are supported by NIH R01HD37047. G.S. is also an HHMI Investigator. U.S.T. and D.P.K. are supported by NIH grant GM033830. All data in the manuscript are available upon request. Researchers can apply to access the microscope as visitors through the Advanced Imaging Center at Janelia Farm (www.janelia.org/aic). Documentation for the construction of a copy of the microscope is available after execution of a research license with HHMI. Portions of the technology described herein are covered by U.S. Patent 7,894,136 issued to E.B. and assigned to Lattice Light, LLC of Ashburn, VA; U.S. Patent 8,711,211 issued to E.B. and assigned to HHMI; and U.S. Patent application 13/844,405 filed by E.B. and K.W. and assigned to HHMI.

SUPPLEMENTARY MATERIALS

www.sciencemag.org/content/346/6208/1257998/suppl/DC1
Supplementary Text
Figs. S1 to S26
Table S1
References (*59*–*73*)
Movies S1 to S18

27 June 2014; accepted 3 September 2014
10.1126/science.1257998

Science
AAAS

Lattice light-sheet microscopy: Imaging molecules to embryos at high spatiotemporal resolution

Bi-Chang Chen, Wesley R. Legant, Kai Wang, Lin Shao, Daniel E. Milkie, Michael W. Davidson, Chris Janetopoulos, Xufeng S. Wu, John A. Hammer III, Zhe Liu, Brian P. English, Yuko Mimori-Kiyosue, Daniel P. Romero, Alex T. Ritter, Jennifer Lippincott-Schwartz, Lillian Fritz-Laylin, R. Dyche Mullins, Diana M. Mitchell, Joshua N. Bembenek, Anne-Cecile Reymann, Ralph Böhme, Stephan W. Grill, Jennifer T. Wang, Geraldine Seydoux, U. Serdar Tulu, Daniel P. Kiehart and Eric Betzig (October 23, 2014)
Science **346** (6208), . [doi: 10.1126/science.1257998]

Editor's Summary

From single molecules to embryos in living color

Animation defines life, and the three-dimensional (3D) imaging of dynamic biological processes occurring within living specimens is essential to understand life. However, in vivo imaging, especially in 3D, involves inevitable tradeoffs of resolution, speed, and phototoxicity. Chen *et al.* describe a microscope that can address these concerns. They used a class of nondiffracting beams, known as 2D optical lattices, which spread the excitation energy across the entire field of view while simultaneously eliminating out-of-focus excitation. Lattice light sheets increase the speed of image acquisition and reduce phototoxicity, which expands the range of biological problems that can be investigated. The authors illustrate the power of their approach using 20 distinct biological systems ranging from single-molecule binding kinetics to cell migration and division, immunology, and embryonic development.

Science, this issue 10.1126/science.1257998

Science (print ISSN 0036-8075; online ISSN 1095-9203) is published weekly, except the last week in December, by the American Association for the Advancement of Science, 1200 New York Avenue NW, Washington, DC 20005.